An Updatable Three-Dimensional Display via Direct Optical Fringe Writing of Computer-Generated Holographic Stereograms in Photorefractive Polymer

by Sundeep Jolly

M.S., Electrical and Computer Engineering
Georgia Institute of Technology (2009)

B.S., Physics
Georgia Institute of Technology (2008)

B.S., Electrical Engineering
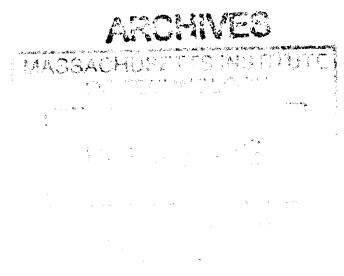Georgia Institute of Technology (2008)

Submitted to the Program in Media Arts and Sciences,
School of Architecture and Planning
in partial fulfillment of the requirements for the degree of

Master of Science

at the

MASSACHUSETTS INSTITUTE OF TECHNOLOGY

September 2012

Author ....

Sundeep Jolly
Program in Media Arts and Sciences
School of Architecture and Planning
September 1, 2012

Certified by ....

V. Michael Bove, Jr., Ph.D.
Principal Research Scientist
Thesis Supervisor
MIT Media Lab

Accepted by ....

Patricia Maes, Ph.D.
Professor of Media Arts and Sciences
Associate Academic Head, Program in Media Arts and Sciences

An Updatable Three-Dimensional Display via Direct Optical Fringe Writing of Computer-Generated Holographic Stereograms in Photorefractive Polymer

by Sundeep Jolly

Submitted to the Program in Media Arts and Sciences,
School of Architecture and Planning
in partial fulfillment of the requirements for the degree of
Master of Science
at the Massachusetts Institute of Technology

Abstract

This thesis aims to assess the feasibility of an updatable three-dimensional display based on the direct fringe writing of computer-generated holographic gratings into a novel photorefractive polymer. The photorefractive polymer in question has been developed by Nitto Denko Technical Corporation and has many attractive properties for the 3-D display application, including long image persistence, rapid erasure, high diffraction efficiency, and large area; however, current holographic display systems based around its use involve interference methods that complicate their optical and computational architectures. The direct fringe writing architecture under question is poised as a simplifying and enhancing alternative to previous demonstrations of updatable holographic displays in photorefractive polymeric materials based around such conventional interference-based holographic stereogram techniques. In addition to simplifying optical architectures, direct fringe writing can allow for complete control of recorded hologram characteristics; interference fringes can be computed to simulate any arbitrary reference beam geometry and wavefront curvature. The system concept – comprised of fringe pattern generation on computer, fringe pattern transfer from SLM to photorefractive polymer, and spatial multiplexing for large-image generation – reintroduces accommodation cues to the resulting holographic images and represents a reduction of system footprint, complexity, and cost relative to the current interference-based systems. The adaptation of the Diffraction Specific Coherent Panoramagram fringe computation method – originally developed to drive AOM-based holographic displays at video rates while preserving all depth cues, including accommodation – to the current display architecture is presented and methods for direct fringe transfer from SLM to photorefractive polymer are depicted. Such methods for direct fringe writing are explored in simulation and experiment. Theoretical arguments for system performance are formulated in the context of a wave optics-based system analysis. Preliminary results of horizontal parallax-only images on this display are presented and directions for performance improvements and system extensions are explored.

Thesis Supervisor: V. Michael Bove, Jr.
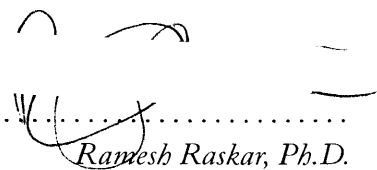Title: Principal Research Scientist

An Updatable Three-Dimensional Display via Direct Optical Fringe Writing of Computer-Generated Holographic Stereograms in Photorefractive Polymer

by Sundeep Jolly

The following person served as a reader for this thesis:

Reader . . . .
Ramesh Raskar, Ph.D.
Associate Professor of Media Arts and Sciences
MIT Media Lab
Massachusetts Institute of Technology

An Updatable Three-Dimensional Display via Direct Optical Fringe Writing of Computer-Generated Holographic Stereograms in Photorefractive Polymer

by Sundeep Jolly

The following person served as a reader for this thesis:

Reader ....

Pierre-Alexandre Blanche, Ph.D.
Associate Research Professor of Optical Sciences
College of Optical Sciences
University of Arizona

Acknowledgments

Contents

List of Figures

List of Tables

Chapter 1

Introduction & Background

1.1 Optical Holography

Holography is a general term referring to the recording and reconstruction of optical wavefronts via interference and diffraction of light. The concept – having been first introduced in its application to microscopy and coined *wavefront reconstruction* by Dennis Gabor in a seminal 1949 paper – has matured considerably over the past several decades and is now widely used for wavefront storage and reconstruction in a variety of applications and domains, including optical metrology, interferometry, imaging, spectroscopy, data storage, computation, pattern recognition, and three-dimensional display [1, 2]. This thesis is focused on the three-dimensional display application.
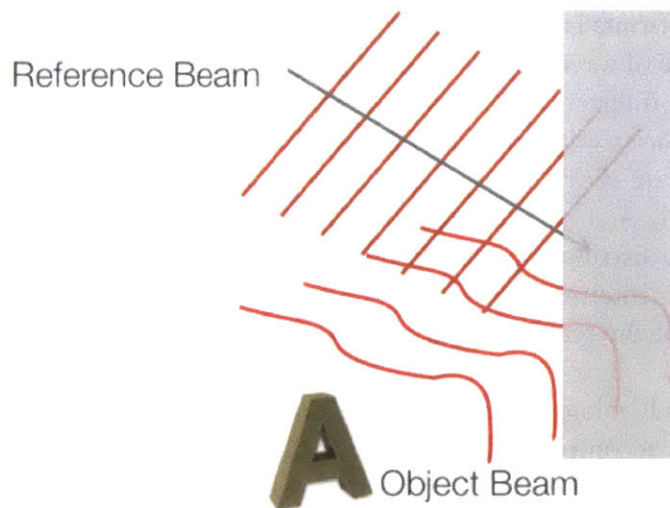
FIGURE 1.1: Recording process for a transmission geometry display hologram. Coherent light scattered from a three-dimensional object interferes with mutually coherent light from a reference beam (depicted here as a plane wave) on the surface or within the volume of a recording medium.
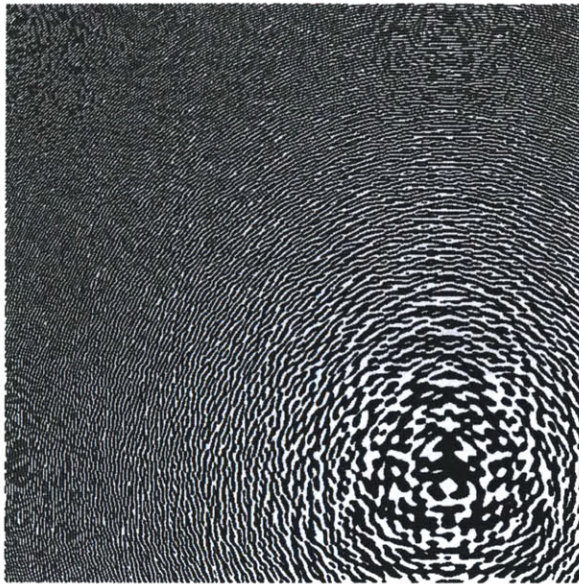
FIGURE 1.2: Typical holographic interfereogram (*fringe pattern*) resulting from the holographic recording process.

In conventional optical recording of display holograms, coherent light scattered from a three-dimensional scene (*object beam*) is added to mutually coherent (*i.e.*, originating from the same coherent source) light from a second beam (*reference beam*); for the case of the display application, this process is depicted in Fig. 1.1. Because of the coherence between the object and reference beams, an interference pattern depending on the relative phases of both incoming wavefronts is formed; this interference pattern is recorded on the surface of or within the volume of a recording material (Fig. 1.2 depicts a representative interference fringe pattern). The interference of the two wavefronts converts relative *phase information* into *intensity information* and therefore holographic recording captures a representation of the *complex optical field distribution* (*e.g.*, $U(x, y) = A(x, y)e^{j\phi(x,y)}$, where $U(x, y)$ is the complex optical field, $A(x, y)$ is the spatial distribution of the scalar field magnitude, and $\phi(x, y)$ is the spatial distribution of field phase) emerging from a three-dimensional scene rather than simply its intensity distribution (*e.g.*, $I(x, y) = |U(x, y)|^2$, where $I(x, y)$ is the spatial distribution of the scalar irradiance) as in conventional photography [3].

In replay of recorded holograms, reconstruction of the wavefront of the original three-dimensional scene is accomplished via illumination of the recorded hologram with a replay beam (depicted in Fig. 1.3). The choice of replay beam depends on the type of hologram being reconstructed (*e.g.*, Gabor in-line, Leith-Upatnieks off-axis, rainbow) as well as the choice of reference beam used during the recording process [4].

Typical optical holographic recording media include dichromated gelatin, silver halide films, photopolymers, photorefractive crystals, and recently, photorefractive polymers [2, 5, 6]. In media such as photographic plates, the incident intensity of the inteferogram typically maps
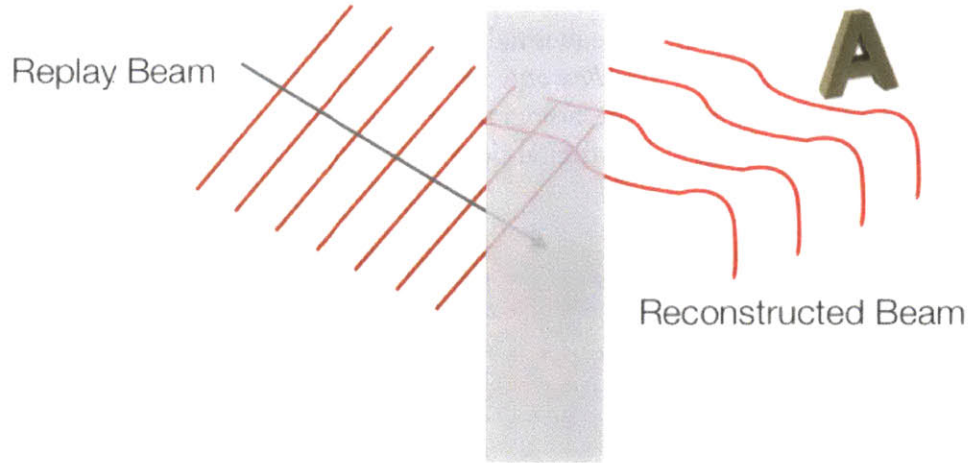
FIGURE 1.3: Reconstruction process for a transmission geometry display hologram. A replay beam is incident on the exposed recording medium, reconstructing the wavefront originally scattered from the three-dimensional object.

linearly into *amplitude modulation* experienced by replay beams during holographic reconstruction and therefore such media carry *amplitude holograms* [3]. Although no recording medium is directly sensitive to the phase distribution of an incident interferogram, many media (*e.g.*, silver halide after bleaching process, dichromated gelatin, most photopolymers, photorefractive crystals and polymers) typically map incident intensity of the interferogram into *phase modulation* experienced by replay beams during holographic reconstruction; these media carry *phase holograms*. Mechanisms for phase modulation vary across types of recording media and tend to be highly nonlinear in their mapping of incident intensity to phase modulation. Photorefractive materials and the photorefractive effect are discussed in further detail in Section 1.6.

1.2 Optical and Digital Holographic Stereogram Printing

Holographic printing, in its modern definition, most commonly refers to schemes for fabricating display holograms from digital three-dimensional scene content, whether from synthetic scenes or real scenes [4]. Modern holographic printing schemes typically employ *holographic stereogram* approaches, in which a 3-D scene is treated as a composition of 2-D images in view angle. Unlike optical techniques for holographic recording, holographic stereogram techniques can allow for a scene to be captured *incoherently* via, *e.g.*, sequential photographs, multi-view camera arrays, or rangefinding cameras [7, 8].

Initial techniques for all-optical holographic stereogram fabrication used "two-step" processes, in which 1) incoherent light is used to record a horizontal sequence of perspective photographs (typically in transparency material) of a three-dimensional scene with equal

spacing between camera positions in the sequence, and 2) the component photographs are holographed (as described below) sequentially onto a holographic recording plate thereby compositing a large *horizontal-parallax only* image [7, 9]. "One-step" techniques followed thereafter and greatly simplified the holographic stereogram recording process [4]. Most modern one-step techniques utilize digital post-processing of perspective images [10, 11].
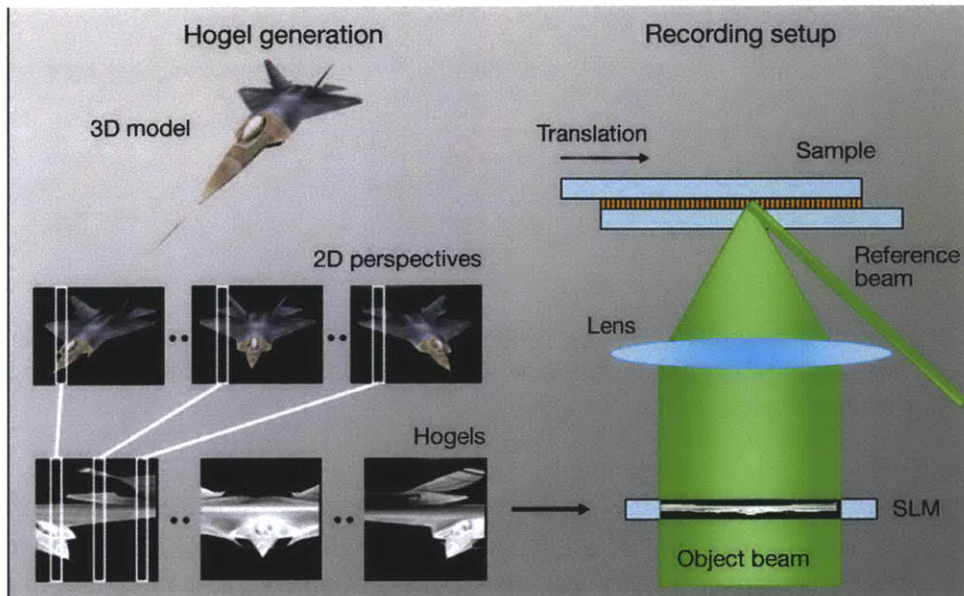
FIGURE 1.4: [Adapted from [13].] High-level overview of "one-step" holographic stereogram printing using the "slice-and-dice" algorithm. Parallax views of a 3-D scene are broken up into segments and assembled into "holographic elements," or *hogels*. Coherent laser light is modulated with hogel information via a spatial light modulator and passed through a lens made to interfere with mutually coherent light from a reference beam or the surface or within the volume of a recording medium, with a lens optically performing Fourier transformation of the hogel information. Optical spatial multiplexing techniques are used to write all hogels corresponding to all scene information in the recording medium.

The conventional holographic stereogram printing process is depicted in Fig. 1.4 for the horizontal-parallax only case. In this scheme, perspective images (*i.e.*, parallax views) of a real or synthetic scene are digitally processed into "holographic elements," or *hogels* and used for stereogram printing as follows:

1. Each component perspective image is broken up into N equally-spaced columns, where N is the total number of perspective images.

2. Each ith hogel is assembled by using the ith column from each perspective image as the nth column in the assembled hogel, where i is the hogel index and n is the perspective image index.

3. Hogels are used to modulate an object beam, which is subsequently passed through a Fourier-transforming lens and made to interfere with a mutually-coherent reference beam on the surface or within the volume of a holographic recording medium. Hogels are printed sequentially and *spatially multiplexed* in order of their indices to raster the entire holographic stereogram. Here, spatial multiplexing refers to the notion of successively positioning different holograms across the recording medium without overlap [12].

This method is often referred to as the "slice-and-dice" approach to hogel generation and holographic stereogram printing; each hogel contains information corresponding to the distribution of intensities over angle [4, 11, 13]. Several practical holographic printers that use this scheme or a variation on it have been developed for both horizontal-parallax and full-parallax imaging.

1.3 Digital Holography

Digital holography can refer to:

1. A variation on the conventional hologram recording technique, in which a digital sensor – typically a charge-coupled device (CCD) or complementary metal-oxide-semiconductor (CMOS) sensor – is used in lieu of a recording medium and thereby the holographic interferogram is captured digitally [14]. The digital interferogram can then be examined in simulation.

2. Techniques for algorithmically-based hologram generation, physics-based simulation, and image reconstruction for computer-generated display holograms, all implemented on digital computers [4].

This thesis will focus on the second item. In tandem with the development of optical-based methods for generating holograms, mathematical- and algorithmically-based methods for holographic fringe pattern generation (*i.e.*, as in computer-generated holograms, or *CGHs*) have matured considerably and are now widely used for creating diffractive optical elements and display holograms [2]. Methods for computer-based display hologram generation include physically-based interference modeling algorithms and diffraction-specific approaches, several of which are now mature enough to support small-scale, video-rate hologram generation [4].

1.3.1 Digital Display Holography: Fourier and Fresnel CGHs

Computer-generated display holograms can be produced with widely varying degrees of fidelity from many types of input source data. Early methods for display CGH generation aimed primarily at image reconstruction in the *Fraunhofer regime* or *far-field* and produced
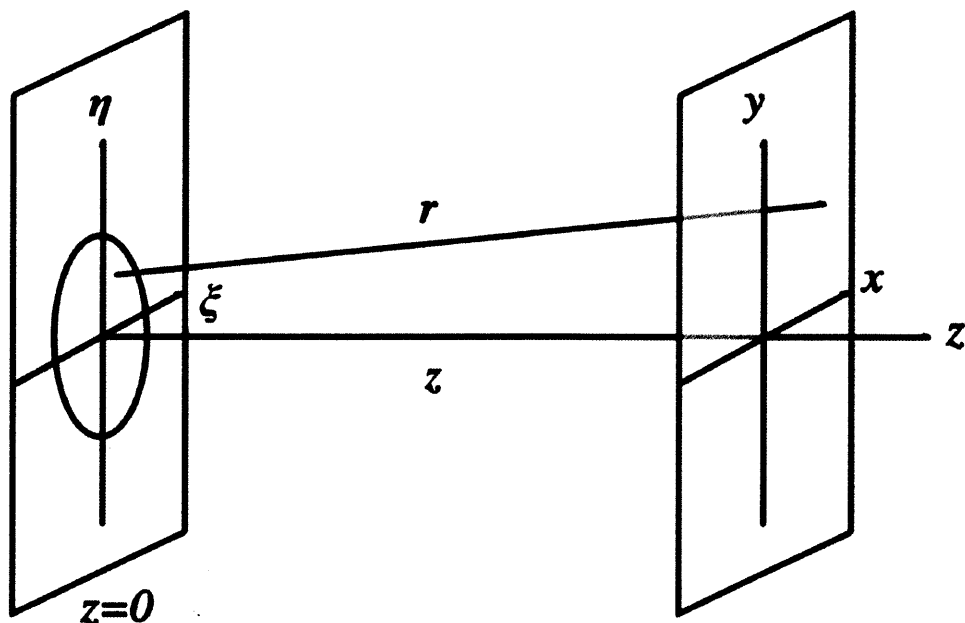
FIGURE 1.5: Diffraction geometry in computational Fourier and Fresnel holography. The diffraction integrals naturally consider the propagation of light from one 2-D plane in space (*input plane*) to another (*output plane*), with separation by a propagation distance z. (ξ, η) are spatial coordinates at the input plane and (x, y) are spatial coordinates at the output plane. For simplicity, the z-coordinate of the input plane is conventionally taken to be 0.

Fourier holograms. These techniques largely derive from inversion of the well-known Fraunhofer diffraction integral:

$$U_D\left(x, y, z\right) = \frac{e^{jkz}}{j\lambda z} e^{\frac{jk}{2z}\left(x^2 + y^2\right)} \int_{-\infty}^{\infty} \int_{-\infty}^{\infty} U_R\left(\xi, \eta\right) t_A\left(\xi, \eta\right) e^{-\frac{j2\pi}{\lambda z}(x\xi + y\eta)} d\xi d\eta \qquad (1.1)$$

where $U_D(x, y, z)$ is the diffracted field (*i.e.*, reconstructed image), λ is the wavelength of the reconstruction beam, $k = 2\pi/\lambda$ is the magnitude of the optical wavevector, z is propagation distance, $U_R(\xi, \eta)$ is the reconstruction beam (typically chosen to be a plane wave), and $t_A(\xi, \eta)$ is the computed Fourier hologram pattern (typically an amplitude-only transmission pattern) [3, 16]. For clarity, a depiction of the diffraction geometry for a Fourier-type hologram is depicted in Fig. 1.5. Examination of the diffraction integral reveals that the requisite transmission function for the Fourier hologram $t_A(\xi, \eta)$ and the desired diffracted field are Fourier-transform pairs, when the reconstruction beam $U_R(\xi, \eta)$ is chosen to be a plane wave. Many such techniques for Fourier-transform based hologram generation were explored; however, Fourier holograms typically suffer from poor image quality, lack of depth in 3-D scene reconstruction, and limited information content and have largely been abandoned as solutions in computational display holography in favor of schemes for fully computing or approximating Fresnel holograms [4].

Most modern techniques for display CGH generation typically aim at image reconstruction in the *Fresnel regime* or *near-field* and produce *Fresnel holograms.* These techniques largely aim at producing holographic fringe patterns suitable for reconstruction in the near-field regime, ideally computed as inversions of the Fresnel diffraction integral:

$$U_D\left(x,y,z\right) = \frac{e^{jkz}}{j\lambda z}e^{\frac{jk}{2z}\left(x^2+y^2\right)} \int_{-\infty}^{\infty} \int_{-\infty}^{\infty} U_R\left(\xi,\eta\right)t_A\left(\xi,\eta\right)e^{\frac{jk}{2z}\left(\xi^2+\eta^2\right)}e^{-\frac{j2\pi}{\lambda z}\left(x\xi+y\eta\right)}d\xi d\eta$$

$$(1.2)$$

where the diffraction geometry and symbolic notations are the same as those in the Fraunhofer integral described above [3, 16]. Examination of this diffraction integral reveals the requisite transmission function for the Fresnel hologram $t_A(x,y)$ cannot be computed simply via inverse Fourier transform of the desired diffracted field for *any* choice of reconstruction beam [4, 15]. This is due to the extra *quadratic-phase exponential* in the integrand, $e^{\frac{jk}{2z}\left(\xi^2+\eta^2\right)}$, which acts to model points in the holographic fringe pattern as *Huygens' wavelets* represented by parabolic-phase emitters and is neglected in the Fraunhofer formulation.

Because of the inherent difficulty in computing Fresnel holograms in an analytically straight-forward manner, many techniques, including physically-based interference modeling and diffraction-specific approaches, have been pioneered as computationally-tractable solutions to the problem [4]. In physically-based interference modeling, the optical interference between 3-D scene points and a simulated reference beam is computed to generate a holographic fringe pattern. These techniques can offer the highest possible fidelity for holographic 3-D scene reconstruction in the Fresnel regime; however, such high fidelity comes at an extremely high computational cost due to the many-to-many calculations and high spatial sampling rates involved [4]. If computational resources (*e.g.*, time, available memory, processing speed) do not pose issues, physically-based interference modeling techniques offer the most "true-to-life" holographic representations of 3-D scenes computationally possible; however, for many applications, the computational burdens are problematic.

1.3.2 Efficient Generation of Digital Display Holograms

In contrast to physically-based interference algorithms for fringe pattern generation, a variety of techniques that take advantage of advances in graphics-processor unit (GPU) rendering and computer graphics to generate holographic fringe patterns with speed and efficiency. Holographic stereogram fringe computation methods aim at computation of fringe patterns similar to those that would result with aforementioned optical holographic stereogram recording techniques and rely on the modulation of pre-computed *basis fringes* with information corresponding to the 3-D scene's content [4, 19]. These basis fringes typically act to emit constant wavefront curvature over all directions, with intensities variable upon scene content.

Diffraction-specific approaches focus primarily on *light field reconstruction* via diffraction from holographic fringes rather than on the physics-based modeling of interference between

scene points and a reference beam and represent a *hybrid approach*, combining elements of physically-based interference modeling with those of holographic stereogram fringe computation (here, *light field* refers to the luminance of all rays in all directions at every point in the scene volume and *not*, e.g., the complex electric field corresponding to an optical wave.) [4, 17, 18]. In contrast to holographic stereogram fringe computation methods, diffraction-specific approaches select basis fringes corresponding to 3-space position of scene object points for modulation rather than simply using constant basis fringe patterns. Relative to physically-based interference algorithms, diffraction-specific algorithms offer greatly reduced computational cost with varying reductions in fidelity. Due to the discretization in space and spectrum inherent to diffraction-specific approaches, such algorithms are most commonly used to generate fringe patterns corresponding more closely to holographic stereograms as opposed to fully-computed Fresnel holograms [4, 19, 22]. Diffraction-specific approaches are computationally efficient enough to provide output fringe patterns for holographic video systems at interactive video rates [19, 21, 22]. Two diffraction-specific approaches that have been developed at the MIT Media Lab for this purpose – the reconfigurable image projection method and the diffraction specific coherent panoramagram method – are utilized in the work contained in this thesis and detailed here.

1.3.3 Reconfigurable Image Projection Holograms

The *reconfigurable image projection* (RIP) method is a diffraction-specific approach to holographic fringe computation that combines elements of holographic stereogram fringe computation with those of physically-based interference modeling to generate holographic images with a more realistic appearance than those generated via conventional holographic stereograms [4, 19, 20]. In the RIP algorithm, chirped gratings corresponding to *directional point emitters* that emit spherical wavefronts are pre-computed, appropriately selected according to the 3-space position of a scene point to be reconstructed, and modulated with the scene point's luminance. This process of chirp look-up and modulation occurs in parallel for all scene points and all modulated chirps are appropriately assembled to create the holographic fringe pattern. The modulation and assembly process is depicted in Fig. 1.6. It should be noted that while images generated using the RIP algorithm can provide suitably correct occlusion, disparity cues, vergence cues, and smooth motion parallax, they *cannot* provide accommodation cues.

The current implementation of the RIP algorithm drives the Mark II electro-holographic video display at interactive rates in a horizontal-parallax only configuration. This entails that the chirped gratings are computed in 1-D and tiled on a line to generate *hololines*. Several such hololines are computed independently over the vertical dimension and tiled to generate the composite HPO holographic fringe pattern corresponding to a scene. The RIP algorithm is implemented via GPU-based shader rendering [21].
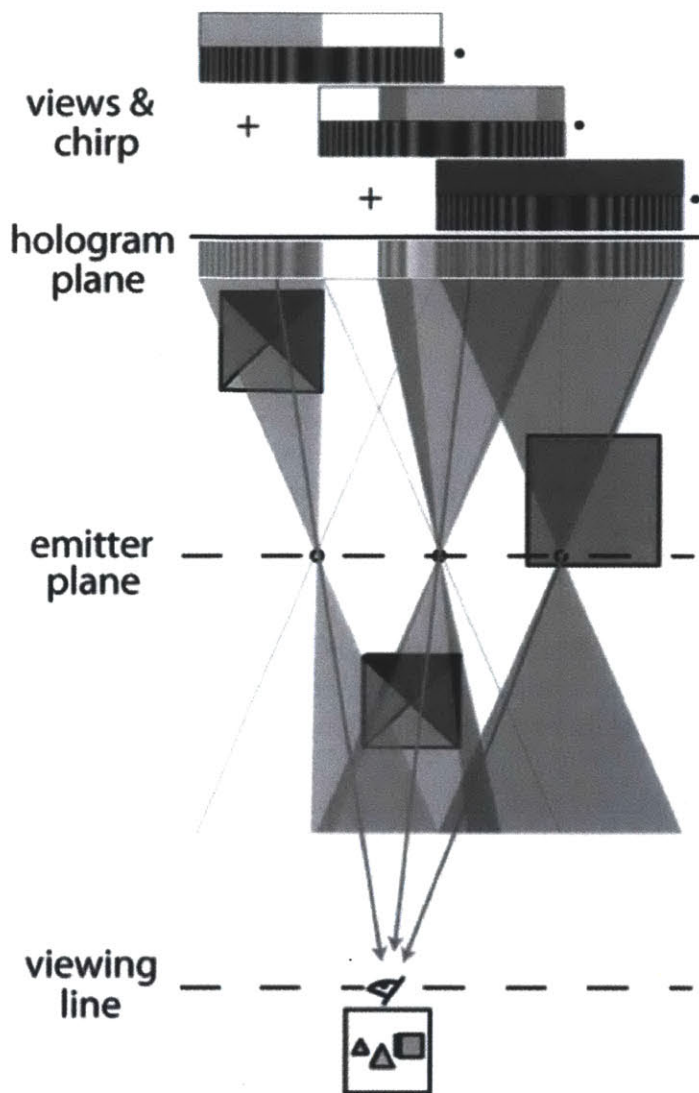
FIGURE 1.6: Assembly process of modulated chirped gratings in MIT diffraction-specific fringe computation methods. 3-space position of a scene point is used to select an appropriate chirped grating for reconstruction which is then modulated with that scene point's luminance information. For HPO imaging, holographic fringe pattern assembly occurs in 1-D.

1.3.4 Diffraction Specific Coherent Panoramagrams

The *diffraction specific coherent panoramagram* (DSCP) is a recent diffraction-specific algorithm for holographic fringe computation developed at the MIT Media Lab [8, 22]. The DSCP is a fast algorithm that can provide for arbitrary (and therefore correct) wavefront curvature in view angle upon reconstruction (and therefore correct visual accommodation cues, unlike many other holographic stereogram and diffraction-specific approaches, including RIP – this limitation of holographic stereograms is explored in detail in Section 2.1) which has originally been developed for use with the MIT Mark II and Mark III electro-

holographic element
hogel

wavefront element
wafel
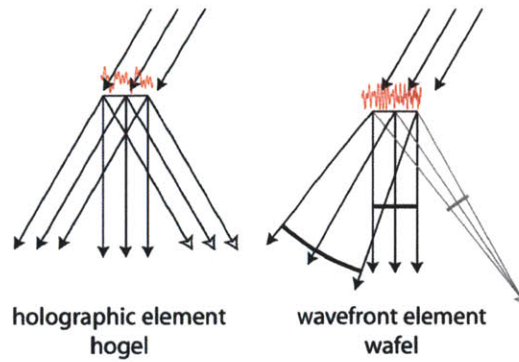
FIGURE 1.7: [Adapted from [22].] Comparative affordances in directional intensity and curvature for the conventional holographic element ("hogel") and the wavefront element ("wafel"). Note that while a hogel emits a series of plane waves in view angle with controllable intensities, a wafel emits a series of wavefronts of *arbitrary, controllable curvature* in view angle also with controllable intensities.

holographic video displays. Remarkably, the DSCP approach can provide smooth motion parallax with *far fewer views* as input to the computation than are required with in conventional holographic stereogram or other diffraction-specific approaches.

In a holographic stereogram, hogels emit an approximation of the ideal wavefront curvature emitted by a 3-D scene via a sequence of plane waves of controllable intensity over view angles. In a diffraction specific coherent panoramagram, *wavefront elements*, or *wafels*, can emit *arbitrary and controllable* wavefront curvatures with controllable intensities over view angles. Fig. 1.7 depicts the differences in the affordances in wavefront curvature provided via hogels and wafels. The wafel's ability to directly generate arbitrary, positionally-variant wavefront curvature (rather than approximate such curvature through the ensemble of many constant-frequency wavelets) allows for better approximation of ideal wavefronts emitted from a 3-D scene (and therefore the DSCP algorithm can provide correct accommodation cues). It should be noted that a diffraction specific coherent panoramagram converges to a fully-computed Fresnel hologram in the limit as the number of views used for computation becomes arbitrarily large.

In the DSCP algorithm, depth information from a 3-D scene (provided via z-buffer information for synthetic scenes or depth camera information for real scenes) is used to appropriately compute holographic basis functions (variable rate chirped gratings, in the current HPO implementation). The chirped gratings are then modulated with the scene luminance information and appropriately tiled to create the complete holographic fringe pattern. This process is similar to the modulated, chirped grating assembly used in the RIP algorithm and depicted in Fig. 1.6.

Fig. 1.8 depicts the comparative accommodation cues provided by a conventional holographic stereogram and those provided by a diffraction specific coherent panoramagram in an experiment that was conducted with the Mark II holographic video display. Two su-
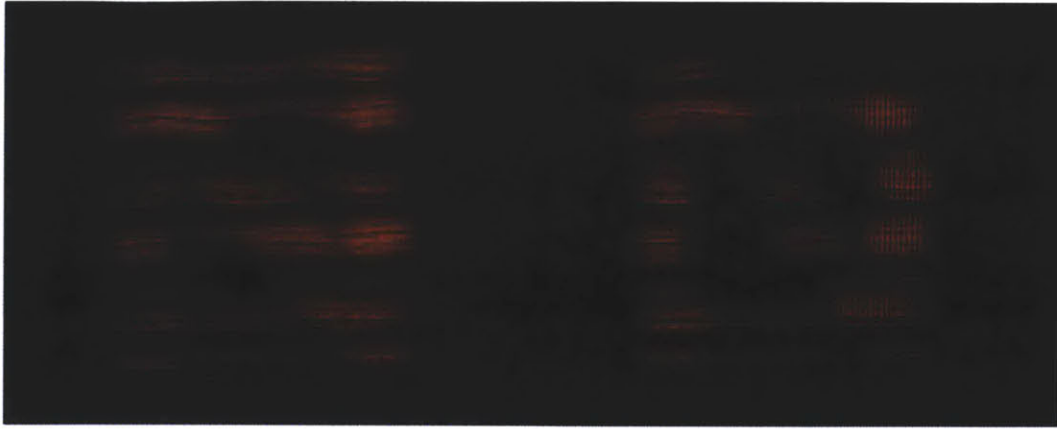
FIGURE 1.8: Comparative accommodation cues in a conventional holographic stereogram (left) and a diffraction specific coherent panoramagram (right). Two letters "D" and "N" are superimposed on one another at varying depths. In the holographic stereogram, the camera cannot disambiguate between the two letters at any focal distance. In the diffraction specific coherent panoramagram, the camera can clearly focus on the letter "N."

perimposed letters "D" and "N" are rendered holographically using both approaches: in the holographic stereogram, the viewer (or camera) cannot disambiguate between the two letters via accommodation but in the diffraction specific coherent panoramagram, the viewer is clearly able to employ accommodation to focus on one letter or the other.

The current implementation of the DSCP algorithm drives the Mark II electro-holographic video display at interactive rates in a horizontal-parallax only configuration. Similarly to the RIP implementation, the DSCP implementation tiles hololines vertically to generate a composite holographic fringe pattern and uses GPU-based shader rendering.

1.4 CGH Fabrication and Direct Optical Fringe Writing

In addition to optical interference-based methods for fabricating holographic gratings, holographic fringe patterns that have been generated synthetically on computer can be *directly* written into photosensitive media. Relative to optical interference-based methods, direct fabrication of digital holograms has several advantages: chiefly, full control over hologram characteristics is afforded through computation rather than through designing an appropriate optical system to generate the necessary interferograms. Electron-beam lithographic techniques are often used for fabrication of holographic optical elements and computer-generated display holograms in massive quantity; however, their use is prohibitive in several applications due to the high cost and specialized equipment involved [23].

Direct optical writing of holographic fringe patterns into photosensitive media has been previously reported in the literature. These schemes consist of 1) display CGH genera-

tion from data from real or synthetic scenes and 2) writing into photosensitive media via pixel-by-pixel (*i.e.*, dot-matrix) approaches or de-magnification of holographic fringe pattern data displayed on SLMs. Matsushima *et al.* demonstrated a direct fringe printer that employed a pixel-by-pixel approach to write CGHs into photosensitive media; the printed holograms were comprised of 8192 x 4096 pixels with anamorphic pixels of dimension 4 μm x 2 μm [24]. Sakamoto *et al.* demonstrated direct writing of CGHs onto recordable compact-disc media in a pixel-by-pixel approach by using a modified CD writer; these holograms exhibit motion parallax in the *rotational* direction about the center of the compact disc and are comprised of pixels of dimension 1.5 μm [25].
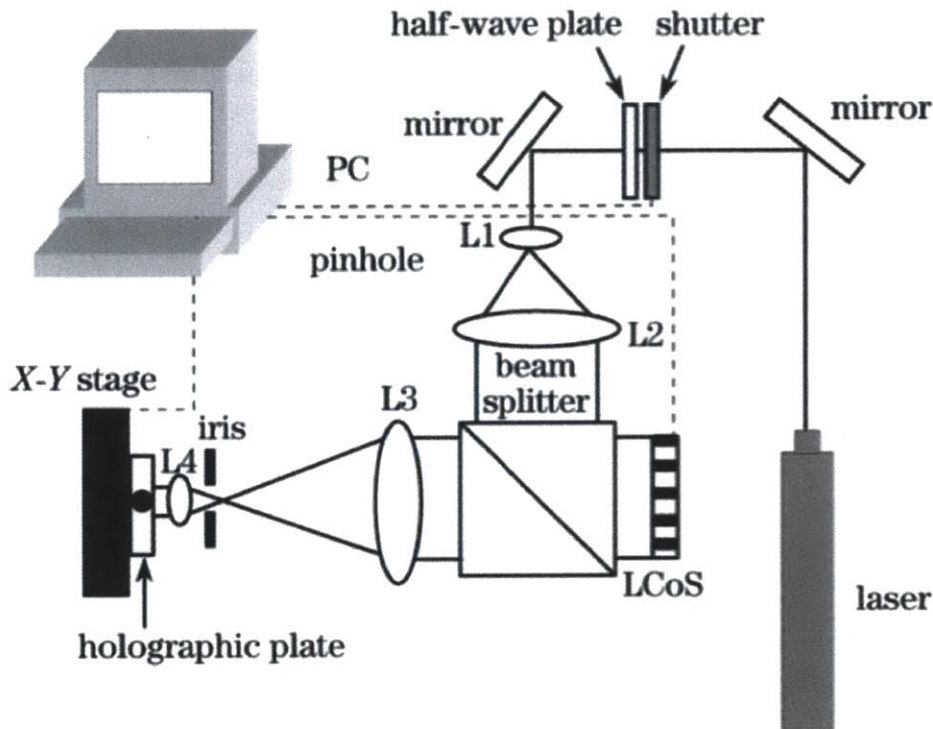
FIGURE 1.9: [Adapted from [26].] High-level schematic of Nihon University direct fringe printer, consisting of liquid-crystal-on-silicon (LCoS) spatial light modulator and de-magnifying optical system. The "area-by-area" approach to holographic printing involves the display of a single "elemental hologram" (not to be confused with holographic element) on the SLM, modulated single-beam exposure of holographic recording medium, translation of recording medium to position for next elemental hologram, and repeat of printing process until all elemental holograms have been rastered into the recording medium.

Yoshikawa *et al.* at Nihon University demonstrated direct optical imaging of fringe patterns displayed on spatial light modulators onto holographic film in a spatial multiplexing approach [23, 26]. This "area-by-area" approach to direct fringe printing breaks up a complete holographic fringe pattern in several "elemental" holograms of resolution equivalent

to that of the SLM. The elemental hologram is used to amplitude-modulate a single beam, which is then passed through de-magnifying optics that act to shrink the effective pixel size prior to exposure on a holographic recording medium in order to increase the viewing angle in reconstruction. In the latest system variant, a nominal pixel size of 0.44 μm at the recording medium has been reported [26].

1.5   Dynamic Holographic Imaging

Dynamic holographic displays have taken advantage of advancements in computer graphics, CGH generation algorithms, and spatial light modulation to generate holographic images that are updatable in real-time (or quasi-real time). Because of the vividness and "true-to-life" nature inherent to high-quality holographic 3-D images, dynamic holography is often viewed as the ultimate form of visual electronic communication. Dynamic three-dimensional holographic displays have a potential wide range of imaging applications in military, medical, and consumer entertainment contexts.
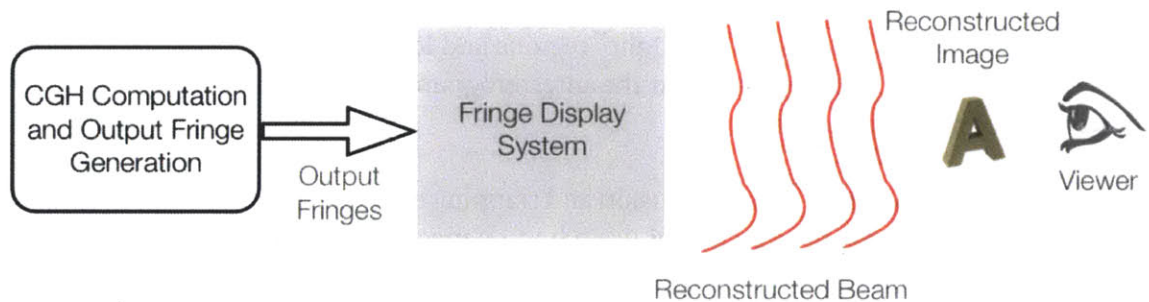
FIGURE 1.10: Generalized system scheme for a dynamic holographic display.

In general, a dynamic holographic display typically consists of a computation scheme for CGH generation and a display device capable of generalized fringe output. This scheme is depicted in Fig. 1.10. Because the smallest effective pixel size that a "fringe output" display can deliver is intricately linked to its maximum available diffraction angle, holographic displays typically need to provide an effective pixel size on the order of the wavelength of the illumination light in order to deliver a convincing holographic image with viewing angle suitable to direct viewing. Because of this requirement, most early implementations of dynamic holographic displays have been limited in size and resolution and to horizontal-parallax only imaging [4].

Dynamic holographic displays are often described as *holographic video* displays and have been based on many different schemes for the needed spatial light modulation. Prior work at the MIT Media Lab has focused on the development of holographic video displays based

around *acousto-optic* modulation of light. At the time of this writing, the Mark II holographic video display is the primary testbed for experiments in horizontal-parallax only dynamic holography at the MIT Media Lab [27].

1.6 Photorefractive Materials for Holography and Nitto Denko Technical Photorefractive Polymer

Photorefractive materials have had a steady history in holographic recording. These materials rely on the so-called *photorefractive effect* as their mechanism for holographic recording. In the photorefractive effect, incident light induces changes in local refractive index (of up to $\Delta n = 10^{-3}$) in electro-optic materials through a process of charge diffusion and trapping (*space-charge field*) [5]. Because of this mechanism, photorefractive materials typically large applied bias voltages to generate base space-charge fields for the photorefractive modulation. Chen *et al.* first realized the potential of photorefractive materials for holographic applications in data storage and display purposes [28]. In photorefractive holographic recording, an incident interferogram (which naturally consists of "light" and "dark" regions with a particular modulation efficiency depending on the object-to-reference beam ratio) induces local refractive index modulation in "light" regions and lesser modulation in "dark" regions; therefore, the intensity information in the interferogram is converted to a phase hologram in the photorefractive material.

Because the mechanism of charge diffusion and trapping exploited in photorefractive recording allows for *release* of trapped charges upon homogeneous illumination, *destructive readout* poses a problem in applications where long or indefinite persistence of recorded holograms is desirable [5, 29, 30]. In applications such as holographic data storage, non-volatile readout can be achieved through methods such as thermally-assisted ionic fixing, spontaneous polarization modulation, or illumination with ultraviolet light during the recording process [29, 30]. However, there are certain application areas (*e.g.*, holographic displays) in which the reversibility of photorefractive materials can be beneficial.

Applications of photorefractive materials to dynamic holographic imaging have historically remained sparse up until recent decades, when novel organic photorefractive polymeric materials emerged [6]. In addition to the properties of fast response time, slow decay time, high index modulation, orientationally-enhanced photorefractivity, and broad spectral response exhibited by several other photorefractive recording materials (*e.g.*, $LiNbO_3$), photorefractive polymers (PRPs) also have the benefit of a large area and therefore have increased utility in the dynamic large-area holographic display application [6, 31].

Recently, researchers at the University of Arizona's College of Optical Sciences and Nitto Denko Technical Corporation (NDT) reported on the development of a photorefractive polymer for dynamic holographic recording having properties including high diffraction efficiency, long image persistence, fast writing, rapid erasure, and large area – a combination
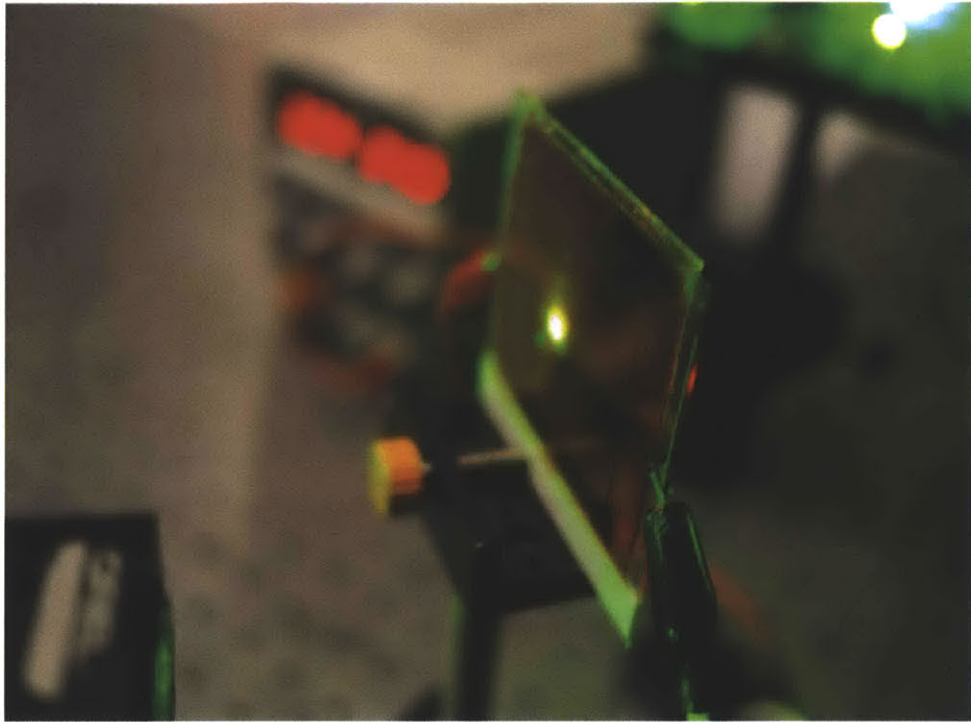
FIGURE 1.11: Photograph of the Nitto Denko Technical photorefractive polymer.

that makes the polymer especially well-suited for application in updatable 3-D holographic displays [13,32–35]. The Arizona-NDT PRP is depicted in Fig. 1.11. At the time of this writing, grating persistence times of up to several hours have been reported [32].

1.7 University of Arizona Photorefractive Holographic Imager

Concurrent with the development of the Nitto Denko photorefractive polymer has been the development of an updatable holographic 3-D display based around the material. [13,32,33]. This development has realized, for the first time, a dynamic photorefractive holographic imager that enables images to be written to the PRP and refreshed as desired, up to a rate of $1/2$ Hz in one of the system variants [33,36]. A high-level schematic of the recording and read-out configurations for the photorefractive holographic imager is depicted in Fig. 1.12. The recording scheme is an instantiation of a "one-step" hogel-based holographic stereogram printer. In this configuration, an object beam is spatially-modulated with hogel information and made to interfere with a mutually coherent reference beam in a Fourier-transform geometry within the volume of the PRP. Spatial multiplexing schemes (as described in Section 1.2) are used to raster the entirety of a holographic stereogram. Recording of new images into the PRP is possible by simply re-writing new information and complete erasure
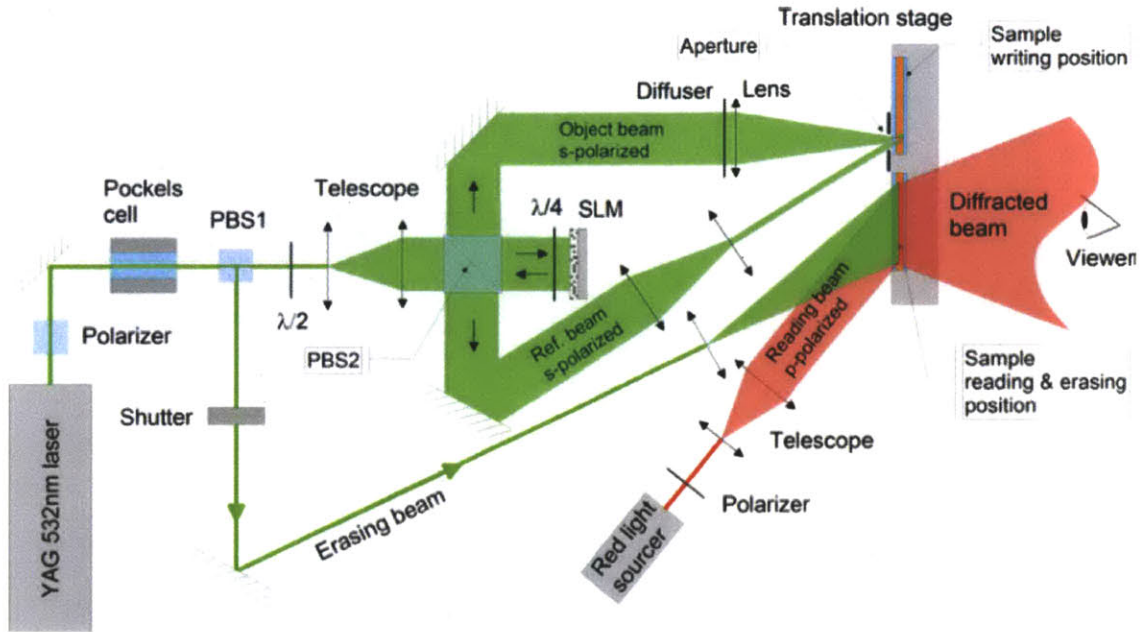
FIGURE 1.12: [Adapted from [33].] High-level optical schematic of the University of Arizona Photorefractive Imager. Coherent laser light at λ = 532 nm is split into an object beam and reference beam. The object beam is modulated with scene hogel information via a spatial light modulator, optically Fourier transformed, and made to interfere with the reference beam within the volume of the photorefractive polymer. Spatial multiplexing is used to raster-scan the entire image. Holographic reconstruction occurs in the transmission geometry, pictured here with a red coherent illumination source.

is possible through homogeneous illumination of the PRP at high optical intensities. Several variants of the photorefractive fringe imager exist, including a slower-update variant employing continuous-wave illumination with hogel exposure time on the order of seconds and a faster-update variant employing pulsed-laser illumination with hogel exposure time on the order of milliseconds.

Because the photorefractive holographic imager uses the conventional holographic stereogram recording process, it is closer in definition to being an *updatable* holographic printing system as opposed to a dynamic holography system based around computed CGH fringe output (as in holographic video systems). In spite of this, update rates of up to 1/2 Hz have been reported and quasi-real-time holographic telepresence has been demonstrated on one of the faster system variants [36]. At the time of this writing, work on the photorefractive holographic imager is progressing and focusing on increasing sensitivity of the photorefractive polymer in order to increase the system update rates [37, 38].

Chapter 2

Motivation & Problem Statement

2.1 Motivation

Because of the combination of developments in novel photorefractive polymers for dynamic holography, demonstrated achievements in direct fringe printing for static holography, and fast methods of fringe calculation in computer-generated display holography, investigation into direct optical writing of computed holographic fringes in photorefractive polymers is merited. Consistent with the ongoing collaboration between MIT and the University of Arizona on holographic display systems, this thesis is aimed at the realization of a proof-of-concept system for updatable three-dimensional display via the direct fringe writing of computer-generated display holograms into the volume of the Nitto Denko Technical photorefractive polymer. With a direct writing scheme, a photorefractive holographic imaging system can be thought of as a (much more flexible) updatable holographic *fringe printer* rather than an updatable holographic stereogram printer.

Direct writing of holographic fringes can potentially provide several benefits to an updatable holographic display based around photorefractive polymeric materials and mitigate several of the limitations of the current systems. Several key advantages are detailed here:

- *Simplification of optical architectures.* Because a direct fringe writing system does not rely on the interference beween an object beam and a reference beam to generate the necessary interferograms for 3-D scene reconstruction, design constraints on the optical architecture of the system are relaxed. Specifically, direct fringe writing eliminates the need for a reference beam and an optical setup capable of producing interference in the photorefractive samples.

- *Reduction of total system footprint.* The current photorefractive holographic imager systems occupy a large footprint and are therefore not easily made portable. A direct fringe writing system can offer reduced system footprint and thereby increase portability.

- *Elimination of need for laser with long coherence length.* In holographic recording, it is necessary that that the individual optical path lengths of both the object and reference

beams from the point of beam-splitting to the point of interference are less than the coherence length of the original coherent source. In the current photorefractive imager, this requirement, coupled with the optical geometry needed to produce the two-beam intereference, entails the use of a laser with long coherence length. In a direct fringe writing system, this requirement is eliminated because the holographic fringe patterns are generated digitally and not via interference. This can potentially allow for the use of a laser source better suited for increased system portability, lower power consumption, and reduced system footprint.

- *Mitigation of scene data requirements.* Holographic stereogram methods, including those currently employed in the University of Arizona photorefractive holographic imager, typically require a large number of densely-sampled parallax views of a scene in order to produce smooth motion parallax in the reconstructed 3-D image. Although CGH methods for generating the fringe patterns needed for holographic reconstruction *do* entail a fringe computation step, there exist methods that can produce smooth motion parallax upon reconstruction with far fewer views than are needed with conventional holographic stereogram techniques (examples and details are provided in Section 4.1).

- *Complete control over characteristics of recorded holograms.* As detailed in Section 1.7, the current photorefractive holographic imager employs conventional holographic stereogram recording methods and is therefore limited in its recording capabilities. Control over the type of holographic fringe pattern recorded would entail changing *optical* parameters of the system, such as reference beam curvature and interference geometry, and is therefore not easily manageable. A direct fringe writing system can allow for vastly increased affordances in the types of holograms that can be recorded: any computable fringe pattern can be recorded in the photorefractive polymer and updated. Direct fringe writing can enable the recording of fringe patterns corresponding to Fourier holograms, holographic stereograms, approximations of Fresnel holograms, and even fully-computed Fresnel holograms. This approach converts the problem of tuning recorded hologram characteristics into a *computational* one rather than an optical one and provides a natural layer of reconfigurability to a photorefractive holographic imager.

- *Introduction of consistent depth cues to reconstructed images.* In a conventional holographic stereogram, a 3-D scene is approximated via the superposition of many 2-D parallax views of that scene in view direction [22]. In the *wavefront reconstruction* picture, the hogels that comprise a holographic stereogram are only controllable in their emitted intensities over angle and *not* in their emitted wavefront curvature (which is limited to planar – this is depicted in Fig. 2.1). Such superposition can provide visual disparity, vergence, and an approximation of smooth motion parallax cues with dense sampling of parallax views but cannot adequately provide visual accommodation cues (due to a lack of precise control over emitted wavefront curvature). Therefore, the depth cues afforded by a holographic stereogram are inconsistent. Because of the
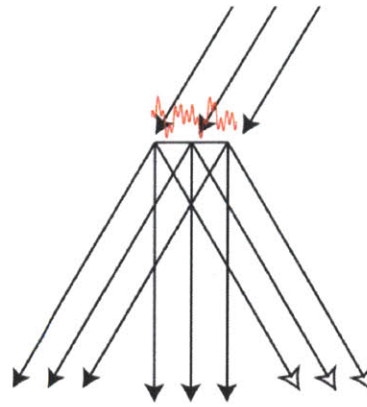
holographic element
hogel

FIGURE 2.1: Hogel reconstruction as a series of plane waves with controllable intensities in controllable directions. Note that while hogels can provide control over emitted wavefront intensity over angle, they *cannot* provide precise control over wavefront curvature and are limited to emitting planar wavefronts.

inherent flexibility in hologram computation, direct fringe writing schemes can reintroduce the missing accommodation cues and provide for smooth motion parallax in reconstructed images, thereby generating more visually consistent holographic reconstructions.

To investigate the extent to which a photorefractive holographic imager can benefit from direct fringe writing, this thesis is part of an ongoing assessment of the feasibility and performance of the direct fringe writing approach with the Nitto Denko photorefractive polymer.

2.2 Challenges

There are several challenges inherent to making direct fringe writing a viable alternative to stereogram-based approaches for holographic recording in photorefractive materials. Several of these challenges are detailed below:

- *Requisite small imaged feature size.* From the simple grating diffraction equation (for the first diffracted order and on-axis illumination, this is $\sin \theta = \lambda/\Lambda$, where θ is the diffracted angle, λ is the illumination wavelength, and Λ is the grating period), we can deduce that smaller feature sizes (*i.e.*, $\Lambda/2$) in a holographic fringe pattern correspond to larger diffracted angles – this relationship is depicted in Fig. 2.2 for the case of the first diffracted order and on-axis illumination. Because of the inverse relationship between diffracted angle and feature size, display holograms with a nominal viewing (*i.e.*, maximally diffracted) angle of 30° require an imaged feature size in the fringe pattern roughly on the order of the illumination wavelength (*i.e.*, $\lambda = 450$ nm to
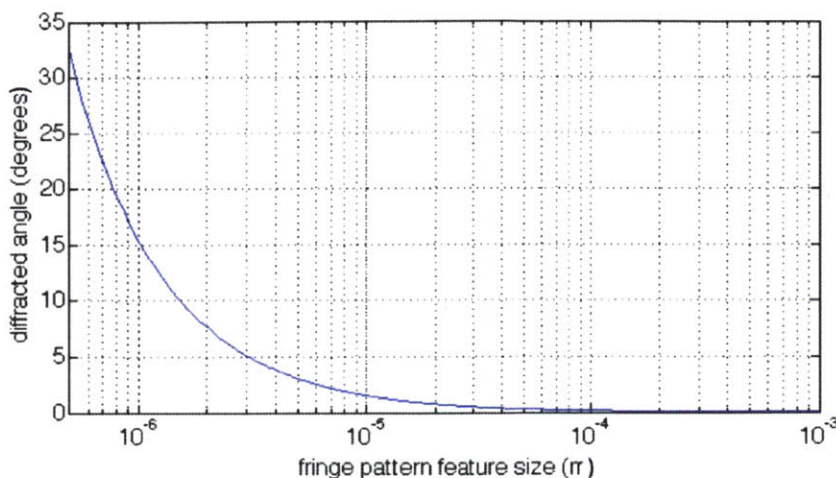
FIGURE 2.2: Maximum diffraction angle possible for given feature sizes (*i.e., grating half-pitch*) in holographic reconstruction. This curve is computed for the first diffracted order and assumes on-axis illumination.

$\lambda = 650$ nm). Given that the smallest pixel size in commercially available spatial light modulators is close to 10x this feature size (*i.e.*, 5 μm), one-to-one imaging of fringe patterns from such an SLM will not produce a hologram with suitable viewing angle for direct viewing and therefore an optical system for imaging fringe patterns is needed and must be capable of the requisite de-magnification and image-space resolution.

- *Requisite large number of pixels for large image reconstruction.* De-magnification of a fringe pattern from a typical commercially-available spatial light modulator (*e.g.*, a liquid-crystal-on-silicon device with resolution 1920x1080 and 8.5 μm pixel pitch) results in an image with reduced dimension of less than 1 mm. In order to achieve a large holographic image, a scheme for spatially multiplexing all parts of a composite large-resolution fringe pattern must be employed.

- *Requisite fringe computation for high perceptual quality of reconstructed image.* In order to faithfully reproduce a 3-D scene, the computed fringe pattern should provide smooth motion parallax and acceptably correct occlusion, accommodation, and vergence cues upon reconstruction.

- *Requisite computational control.* A computational control scheme must be developed to handle all aspects of system operation, including fringe computation, exposure control, and spatial multiplexing (*i.e.*, raster scanning).

Candidate solutions to these issues and an overall system concept for direct fringe writing in the photorefractive polymer are presented in Chapter 3.

36

2.3   Problem Statement & Scope

This thesis is aimed at investigating candidate approaches for handling issues listed in Section 2.2 as well as developing a proof-of-concept direct fringe writing display system for comparison to the existing display systems based around this photorefractive polymer. This thesis is framed as part of a larger *feasibility study* for the direct fringe writing approach.

While the ultimate goal of this endeavor is to realize a direct fringe writing system that meets or exceeds the performance metrics (*e.g.*, diffraction efficiency, size of 3-D image, writing speed, perceptual quality of 3-D image) of the current interference-based systems while reducing system complexity and cost, the scope of the work presented in this thesis has been limited from that ultimate goal and encompasses only initial system build-up, modeling & simulation efforts, and experimentation commensurate with the goal of assessing primary feasibility. For the feasibility assessment, display architectures are limited to horizontal-parallax only imaging.

Higher-level objectives of this work that are outside the scope of this thesis and possible extensions are detailed in Chapter 6.

Chapter 3

System Concept & Experimental Methods

3.1 High-Level System Overview
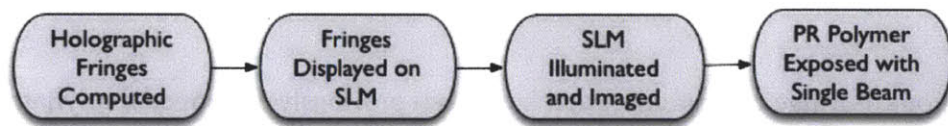
FIGURE 3.1: High-level system overview for direct optical fringe writing in photorefractive polymer. The direct fringe writing scheme is comprised of 1) holographic fringe computation, 2) fringe display on spatial light modulator, 3) modulation of single beam with fringe information and de-magnification via imaging optics, and 4) exposure of photorefractive polymer with single modulated, de-magnified beam. It should be noted that steps 2 - 4 represent one "cycle" of an overall spatial multiplexing loop that progresses until the entirety of the computed holographic fringes are written into the photorefractive polymer.
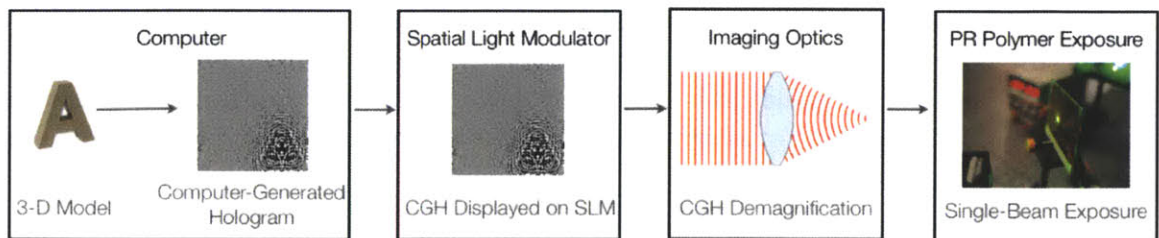
FIGURE 3.2: Component-level system overview for direct optical fringe writing in photorefractive polymer.

The high-level approach to investigating feasibility of direct fringe writing is depicted in Figs. 3.1 and 3.2 and involves the computation of fringe patterns, division of holographic

fringe patterns into "elemental" holograms, display of elemental fringe patterns on spatial light modulator, transfer of fringe patterns from spatial light modulator to photorefractive polymer via de-magnifying optics, and spatial multiplexing for large-image generation. In general, a large resolution holographic fringe pattern is fully computed and broken up into several "elemental" fringe patterns (each of which has resolution equal to the chosen SLM's native resolution). The system then enters into a spatial multiplexing loop, in which the photorefractive polymer is exposed with each (optically imaged) elemental fringe pattern with appropriate re-positioning (*i.e.*, in a raster scan) of the photorefractive polymer in between exposures until the total composite fringe pattern has been written. Details of the methods used for fringe computation, spatial light modulation, optical imaging, and spatial multiplexing are presented here.

3.2 Fringe Computation

Two methods of fringe computation that have been previously developed for dynamic HPO holographic imaging on MIT holographic video displays are presented here in their adaptation to this fringe writing architecture. These methods – the Reconfigurable Image Projection Hologram (RIP) method and the Diffraction Specific Coherent Panoramagram (DSCP) method – have been previously detailed in Section 1.3.

Note that the DSCP algorithm offers several advantages over both the existing interference-based holographic stereogram recording and CGH stereogram fringe computation methods and is used to demonstrate the advantages of direct fringe writing. Furthermore, the choice to use the DSCP rather than, *e.g.*, a more accurate full Fresnel hologram computation is largely based on its speed and efficiency. Because of limitations on writing speed, the direct fringe writing system under investigation in this thesis is not capable of taking full advantage of the computational efficiency of the DSCP. In spite of this, the use of DSCP is merited for this feasibility study as it can support future quasi-real-time fringe computation in an future implementation of a high update rate photorefractive holographic imager based around direct fringe writing.

The adaptation of the RIP and DSCP fringe computation methods to the photorefractive direct fringe writing imager retain their on-GPU, shader-based implementations. While these algorithms have originally been developed to drive holographic video displays in real-time, fringe patterns are "pre-computed" from computer graphics models and computed for horizontal-parallax only imagery for this feasibility study. Specifics of imagery and computed fringe pattern resolution are presented in Chapter 6.
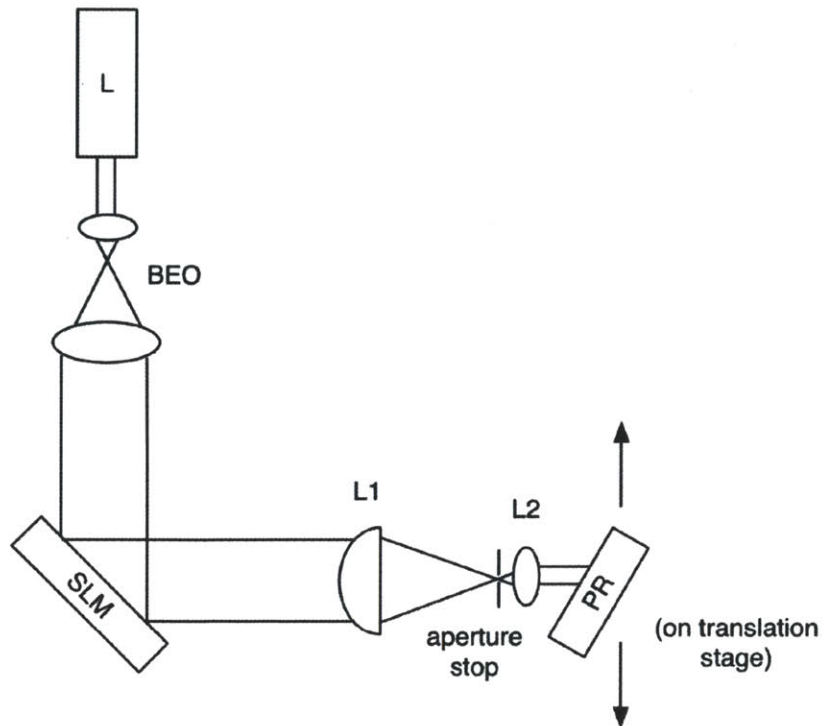
FIGURE 3.3: Schematic of optical system. L = continuous-wave laser at $\lambda = 532$ nm, BEO = beam-expanding optics, SLM = LCoS spatial light modulator, L1 = first cylindrical lens of telecentric optical system with $f = 250$ mm, L2 = second cylindrical lens of telecentric optical system with $f = 50$ mm, PR = photorefractive polymer (on translation stage for spatial multiplexing).

3.3   Experimental Setup

3.3.1   Optical Setup

Direct fringe writing affords a simplified optical architecture in contrast to those necessitated by interference-based holographic stereogram recording schemes. The optical architecture used for the current writing scheme is depicted in Figs. 3.3 and 3.4. The writing system is comprised of a solid-state, diode-pumped continuous-wave laser at $\lambda = 532$ nm, beam-expanding optics, liquid-crystal-on-silicon (LCoS) spatial light modulator in cross-polarizer configuration, bilaterally-telecentric optical system for fringe pattern transfer and demagnification, motorized translation stage for spatial multiplexing, and photorefractive polymer.

In this setup, the LCoS SLM displaying a fringe pattern to be written in the photorefractive polymer is illuminated with collimated, beam-expanded monochromatic laser light originating from a Coherent Verdi V-2 solid-state, diode-pumped, tunable power laser at $\lambda = 532$ nm. In a cross-polarizer configuration, the LCoS device acts as an amplitude-only modulator (details in section 3.3.2). The modulated beam is then incident on the bilaterally-

FIGURE 3.4: Photograph of the direct fringe writing setup. Left: DPSS laser, beam-expanding optics; center: LCoS SLM in cross-polarizer configuration; right: telecentric imaging optics and photorefractive polymer.

TABLE 3.1: Optical system parameters for direct fringe writing testbed.

Illumination Source	Continuous-wave at $\lambda = 532$ nm
L_1 focal length	250 mm
L_2 focal length	50 mm
Peak Irradiance	0.75 W/cm^2
Nominal De-magnification	5x, horizontal-only
Nominal Pixel Size at PRP	1.7 μm
Maximal Irradiance at PRP	2.5 W/cm^2

telecentric optical system comprised of two cylindrical lenses, with de-magnification (equivalent to the ratio of focal length of the second lens to that of the first lens, *i.e.*, $M = f_2/f_1$) occurring in the horizontal direction only. The telecentric imaging system provides an image with nominally propagation-invariant field size after exit from the system and nominally infinite focus (although in practice there is a noticeably finite depth of focus). The particular optical system parameters used here are listed in Table 3.1. It should be noted that the distance between lenses L_1 and L_2 is given by the sum of their focal lengths, *i.e.*, $f_1 + f_2$, and the aperture stop is placed between the two lenses at a distance f_1 from the first lens and f_2 from the second lens. Note that the nominal pixel size arriving at the photorefractive polymer arises from the nominal de-magnification of the telecentric optical system and the pixel pitch of the SLM (detailed in the following subsection). The maximal irradiance listed for exposing the photorefractive polymer arises from the maximal safe output power of the laser and assuming the SLM displays an "all-pixels-white" pattern, allowing the maximal spatial

irradiance distribution to pass to the optical imaging system and photorefractive polymer.
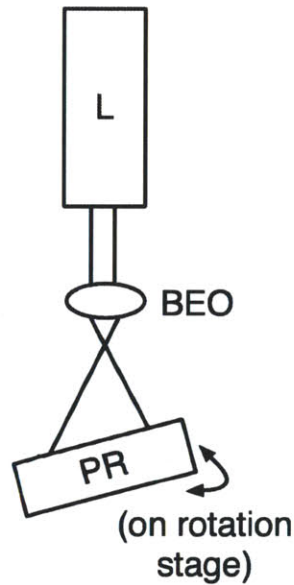
FIGURE 3.5: Schematic of illumination system. L = continuous-wave laser at $\lambda = 632.8$ nm, BEO = beam-expanding optics, PR = photorefractive polymer.

The readout system employs an expanded beam from a continuous-wave laser at $\lambda = 632.8$ nm for illumination and is depicted in Fig. 3.5. The beam is expanded through an optical spatial filter with magnification power 30x.

3.3.2 Spatial Light Modulation

For the current study, liquid crystal-on-silicon (LCoS) SLM panels furnished by Silicon Micro Display are used. These LCoS panels have 88% fill factor and 8.5 μm pixel pitch at a resolution of 1920x1080 (see Fig. 3.6) and are driven with standard PCs over HDMI input. For amplitude modulation, the LCoS device is used in a cross-polarizer configuration (depicted in Fig. 3.7) in which a polarizer is placed before the SLM to generate the proper polarization state (with alignment parallel to the native liquid crystal axis) and an analyzer is placed after the SLM to retrieve the modulated state. In the current configuration, the polarizer and analyzer are laminated film.

43
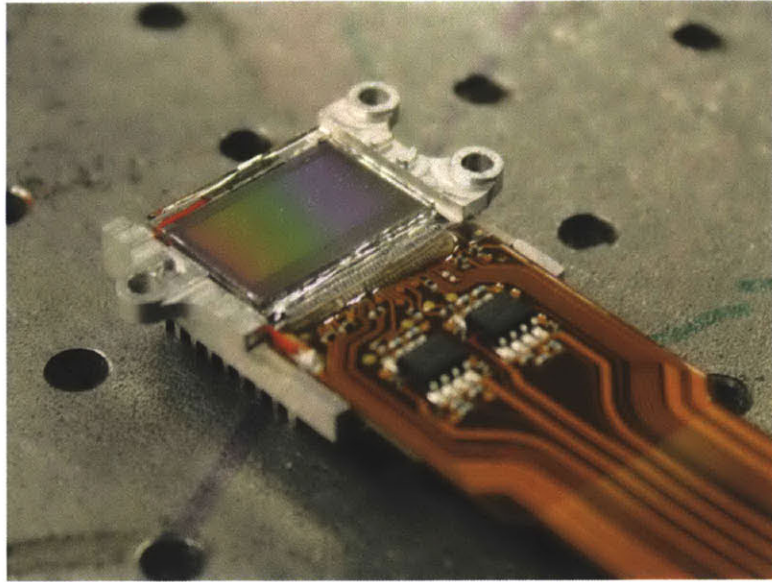
FIGURE 3.6: Photograph of the Silicon Micro Display liquid-crystal-on-silicon module.
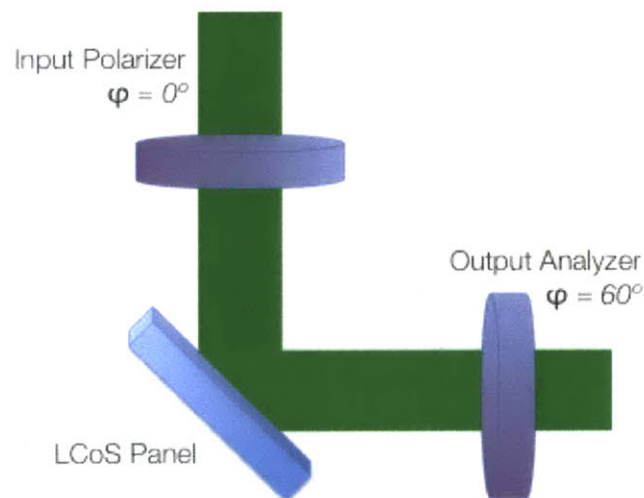
FIGURE 3.7: Cross-polarizer configuration to retrieve amplitude modulation. The input polarizer has its axis parallel to the native liquid-crystal axis of the LCoS device and the output analyzer has its axis oriented at 60° relative to the native liquid-crystal axis.

3.4 Spatial Multiplexing

The total number of fringe pattern content that can be written in a single exposure is limited by the resolution of the SLM. Because the overall number of pixels in a computed HPO holographic fringe pattern is many times larger than that available for use on a single SLM, spatial multiplexing is needed to fully-raster the entirety of the HPO fringe pattern into the photorefractive polymer. This involves 1) segmentation of the fully-computed HPO fringe
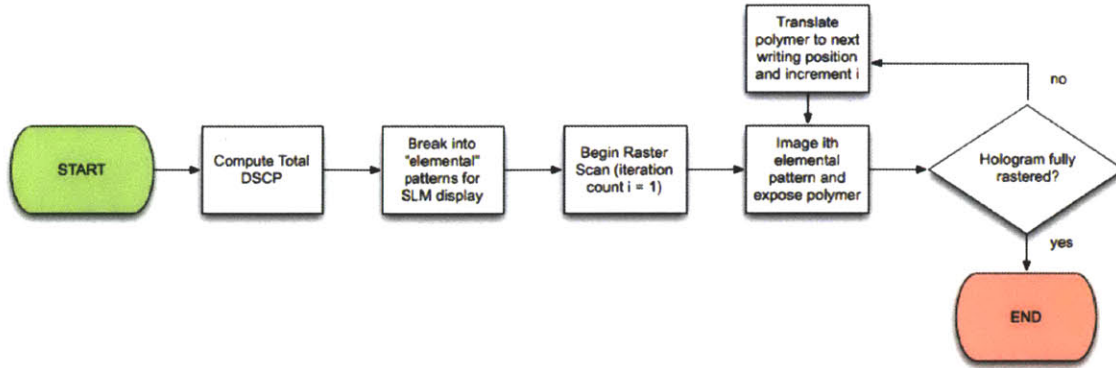
FIGURE 3.8: Process flow of the spatial multiplexing scheme for fully-rastering a complete HPO holographic fringe pattern into the photorefractive polymer.

pattern into "elemental" fringe patterns having resolution less than or equal to that of the SLM, 2) sequential display of elemental patterns on SLM and exposure of photorefractive polymer with elemental information, 3) translation of photorefractive polymer for exposure of subsequent elemental patterns, and 4) repetition of steps 2-3 until the fringe pattern is fully rastered. This scheme is depicted in Fig. 3.8.

The initial process of segmentation of the full HPO fringe pattern involves "slicing" the fringe pattern into segments of width equal to that of the SLM resolution (1920 pixels, for the current SLM – also note that fringe patterns are computed to have a vertical dimension less than that of the SLM). The HPO holographic fringe pattern of pixel width P is segmented into N elementals, each having a pixel width p equal to that of the SLM being used and where N is $\lceil P/p \rceil$. This process is depicted in Fig. 3.9.

In organic photorefractive polymers, a projection of the applied electric field in the direction of the grating vector is needed to generate the space-charge field; therefore, the surface normal of the photorefractive polymer must be obliquely slanted relative to the writing beam's propagation direction for photorefractive modulation to occur [31, 38]. This optimum *projection angle* has been empirically determined to be between 30° and 45°. The photorefractive polymer is on a motorized translation stage for spatial multiplexing. This stage affords travel in the $\hat{x}$ and $\hat{z}$ axes. Because of the slant angle, ensuring that each spatially-multiplexed exposure happens at a constant plane in $\hat{z}$ is projection to ensure uniformity across the fully-rastered fringe pattern and involves translating the polymer in $\hat{z}$ by a distance $\Delta z = \Delta x \tan\theta$ (where θ is the slant angle) for each translation step in $\hat{x}$ of Δx. This process is depicted in Fig. 3.10. Note that while translation in a single-axis *parallel* to the photorefractive polymer would accomplish the same positioning, the current two-axis configuration was chosen for ease of re-configurability with respect to changing the projection angle (*i.e.*, adjusting a translation step in software rather than re-orienting and re-aligning a translation stage with respect to an optical path).

Fully-Computed HPO Fringe Pattern

Segmentation into "Elemental" Fringe Patterns

Elemental Fringe Patterns
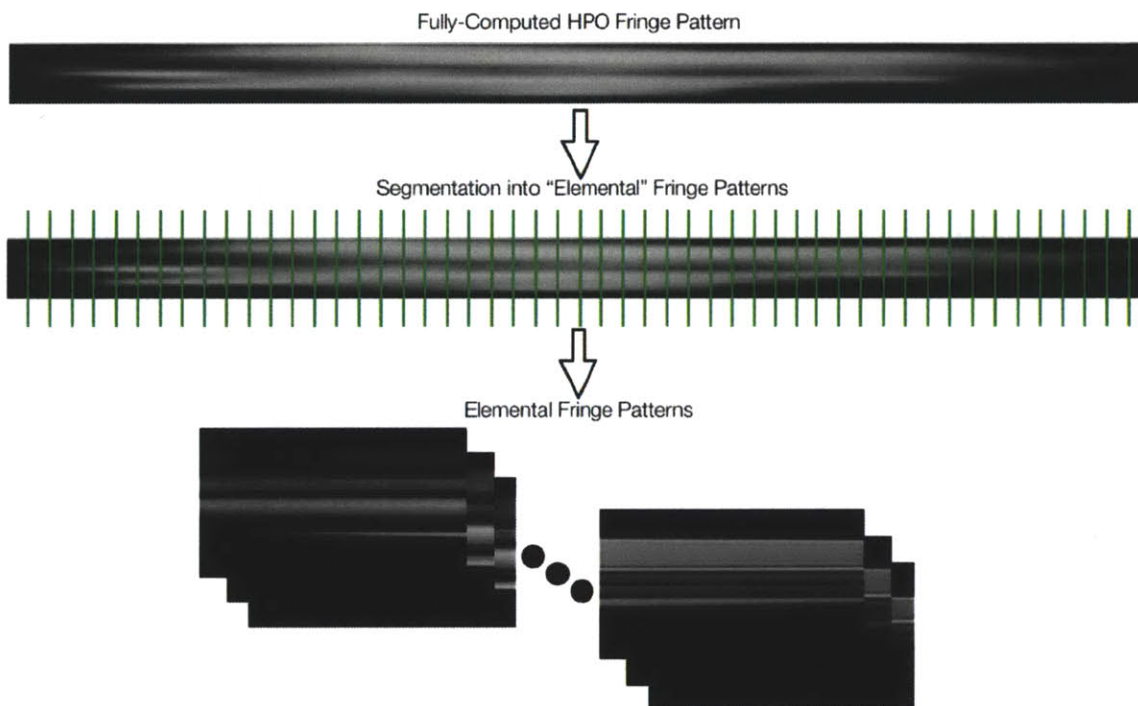
FIGURE 3.9: Process flow of segmentation of a fully-computed horizontal-parallax only holographic fringe pattern into "elemental" holograms for display on spatial light modulator and direct writing into photorefractive sample. The HPO holographic fringe pattern of pixel width P is segmented into N elementals, each having a pixel width p equal to that of the SLM being used and where N is $\lceil P/p \rceil$. Note that the aspect ratio of HPO fringe pattern pictured here has been modified from its original 25:1 to accommodate this illustation.
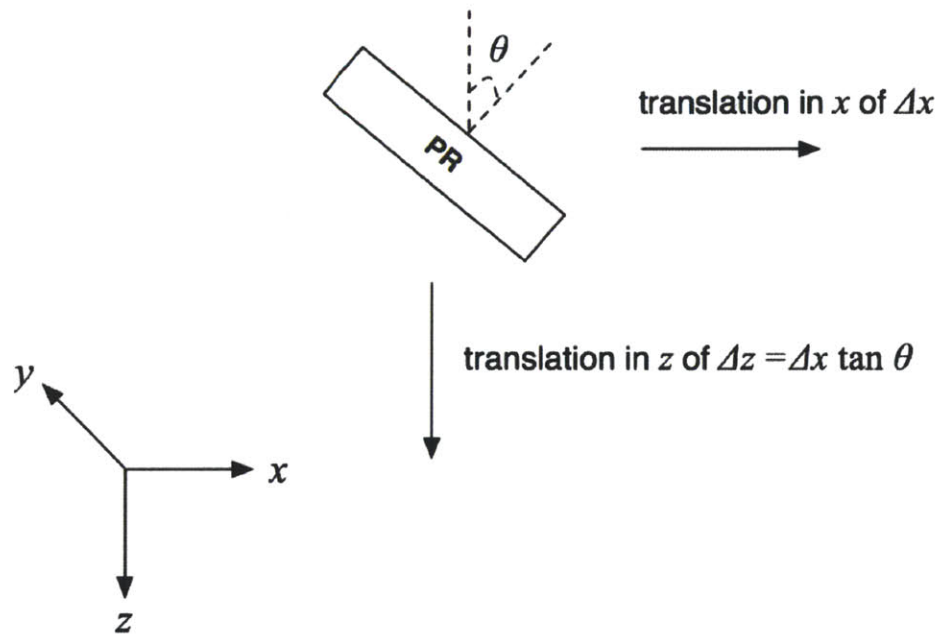
FIGURE 3.10: Depiction of slanted photorefractive polymer geometry in spatial multiplexing scheme. To enforce a constant plane in $\hat{z}$ for exposure at all points during the multiplexing process, a translation step of Δx (*i.e.*, the width of each imaged elemental on the photorefractive polymer) in $\hat{x}$ is accompanied by a corresponding step of $\Delta z = \Delta x \tan \theta$ in $\hat{z}$, where θ is the projection angle of the photorefractive polymer relative to the optical axis z.

3.5   Top-Level Control
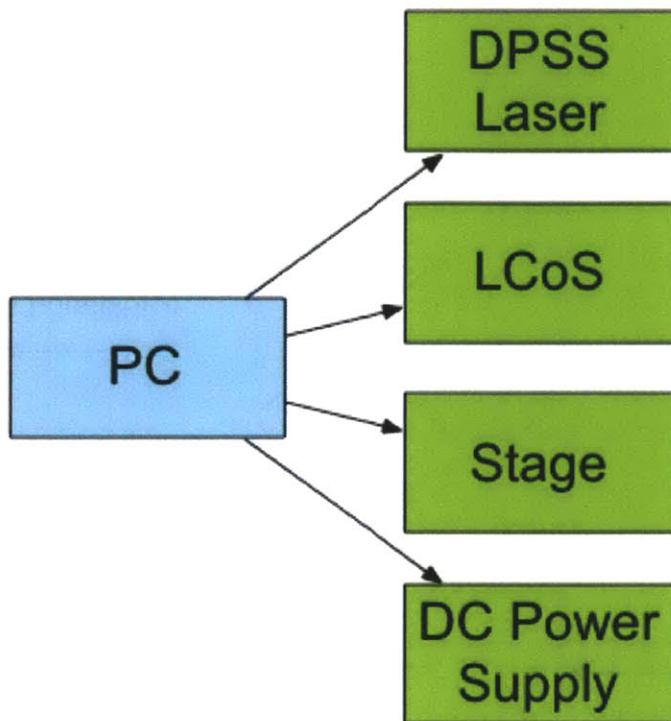
FIGURE 3.11: Top-level control scheme, in which a PC running NI LabVIEW 2011 interfaces with the DPSS laser (for power and shutter control), LCoS device (for displaying fringe patterns), translation stage (for translating the photorefractive polymer appropriately during the spatial multiplexing process), and DC power supply (for providing the correct bias voltage to the photorefractive polymer).

Top-level control of the system is necessary to coordinate all aspects of the direct fringe writing process. A PC running the NI LabVIEW 2011 package is used to interface with the DPSS laser (for power and shutter control), LCoS device (for displaying fringe patterns), translation stage (for translating the photorefractive polymer appropriately during the spatial multiplexing process), and DC power supply (for providing the correct bias voltage to the photorefractive polymer). This scheme is depicted in Fig. 3.11.

The NI LabVIEW 2011 package is used to interface with all instruments. The implemented Virtual Instrument (VI) allows for control over translation steps during spatial multiplexing, laser power during exposure, exposure time, initial positional offsets of the photorefractive polymer, and bias voltage for the photorefractive polymer. The front panel of the VI is shown in Fig. 3.12 and the complete block diagram is provided in Appendix A.
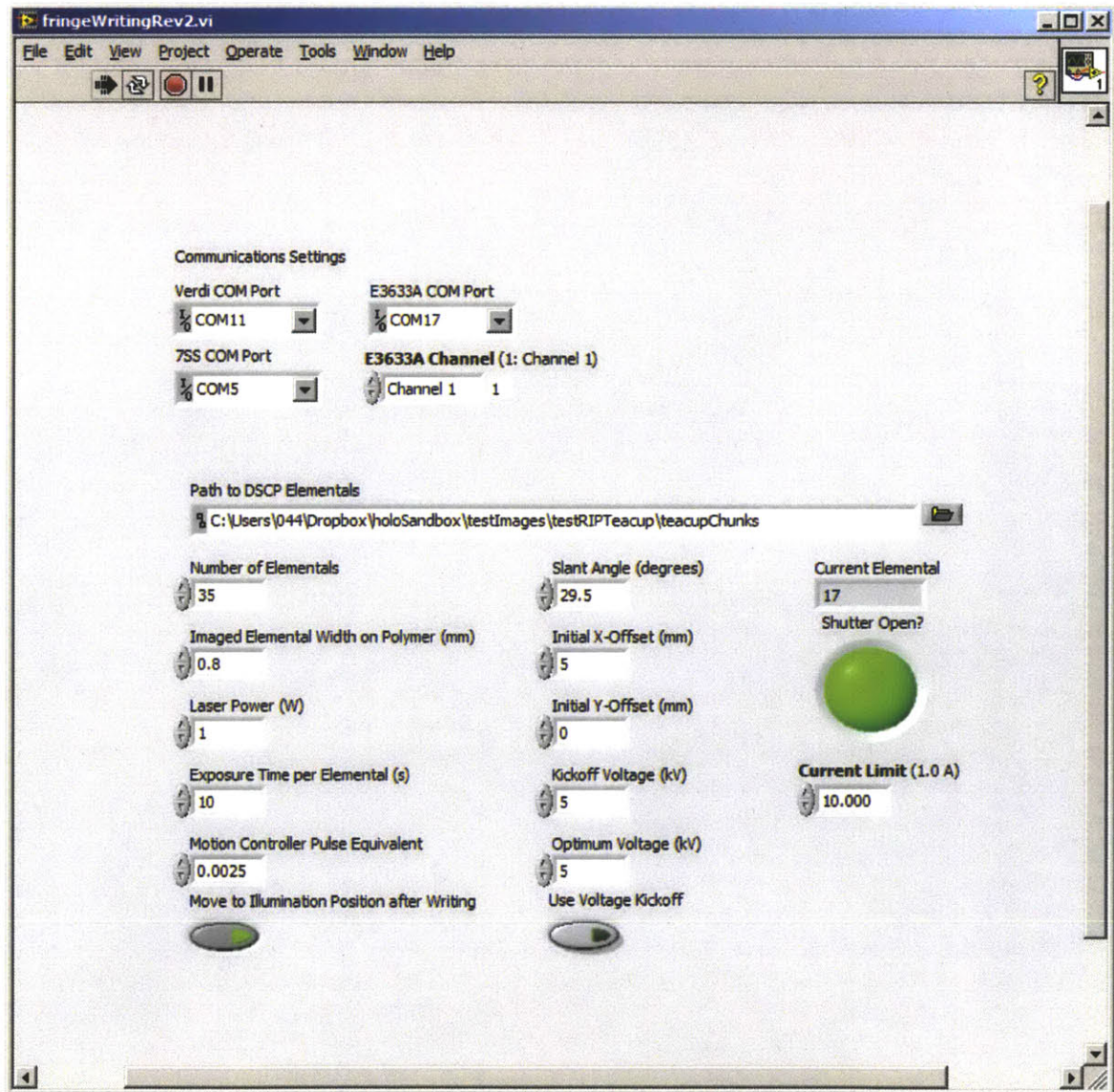
FIGURE 3.12: Front panel of implemented LabVIEW Virtual Instrument for system control. The Virtual Instrument provides control over exposure irradiance, exposure time, photorefractive polymer external field, positioning for spatial multiplexing, and elemental fringe pattern data.

Chapter 4

Optical Modeling, Simulation & Characterization

Recording Geometry

Replay Geometry
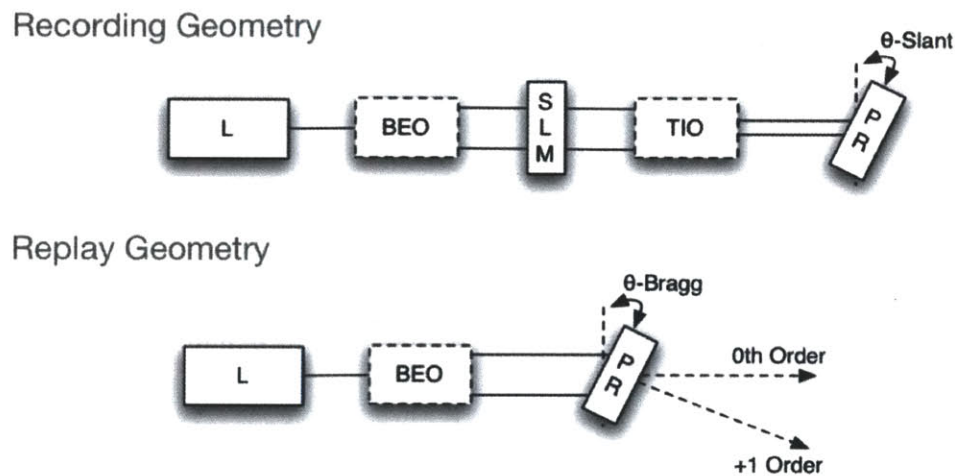
FIGURE 4.1: Generalized system block diagram for optical modeling and characterization. "L" is a monochromatic laser light source, "BEO" is a system for beam-expanding optics, "SLM" is the spatial light modulator, "TIO" is a system for telecentric imaging optics, and "PR" is the photorefractive polymer.

End-to-end optical modeling and simulation is necessary to identify factors negatively affecting system performance as well as to aid in characterizing overall system performance. For purposes of modeling and simulation, the recording process is considered separately from the readout process. In Fig. 4.1, the discrete system "blocks" that the system is segmented into for optical modeling into are depicted. Optical modeling is carried out using MATLAB and ZEMAX optical design software.

For the current study, optical modeling and simulation is used primarily to investigate the theoretical performance of the *imaging* system, in comparison to an ideal one. The current model involves the use of *test gratings* as the fringe patterns for direct fringe writing; modeling with holographic fringe patterns corresponding to 3-D images is outside the scope of

this thesis. Because the scope of this model is limited, many factors that may influence the overall performance of the real system are not considered; these limitations are discussed in Section 4.3.

4.1 Imaging System Characterization

Characterization of the imaging system involves analysis of the quality of image transfer from SLM to photorefractive polymer. ZEMAX optical design software is used for optical design and simulation, specifically in characterization of the system's *point spread function* (PSF) and *modulation transfer function* (MTF). The imaging system corresponding to the real experimental setup described in this thesis is implemented in ZEMAX using stock lens files corresponding to singlet cylindrical lenses with the dimensions and surface curvatures of those used in the real setup.

The point spread function of an optical imaging system describes its *impulse response* (*i.e.*, the image the optical system forms of a point source) [3]. The "cleanliness" with which the point spread function depicts the image of a point source can indicate the degree to which aberrations, diffraction, or other non-idealities of the imaging system negatively affect the system performance. In treating the imaging system as a linear shift-invariant system, the point spread function can be numerically convolved with input images (*i.e.*, input optical fields) to yield the output images (*i.e.*, output optical fields).

The modulation transfer function of an optical imaging system describes the contrast with which features of a given spatial frequency in the input plane will be imaged at the output plane (relative to their original contrast) and is the counterpart to the point spread function in the spatial frequency domain [3]. High *modulation transfer* is typically of interest when imaging progressively smaller features as most imaging systems act as *low-pass* filters in the spatial frequency domain and smaller feature sizes are imaged with lower contrast. As described in Section 2.2, direct fringe writing necessitates the writing of small feature sizes (ideally on the order of 1 μm or less) into the photorefractive polymer to achieve an image viewing angle suitable for direct viewing. For the imaging system being considered here, the modulation transfer function is depicted in Fig. 4.2.

4.2 Wave Optics Model

To model the exposure of the photorefractive polymer, the electric field distribution at all points within the volume of the photorefractive polymer needs to be known. In the top portion of Fig. 4.1, this involves modeling the evolution of the field through its plane wave initialization (the field incident on the SLM, emerging after the BEO block), spatial light modulation and propagation to the entrance pupil of the telecentric imaging system, transformation by the telecentric imaging system, and propagation into the photorefractive material. This process of modulation, transformation, and propagation is described in Section 4.2.1 and the process of exposure of the photorefractive polymer by the incident field
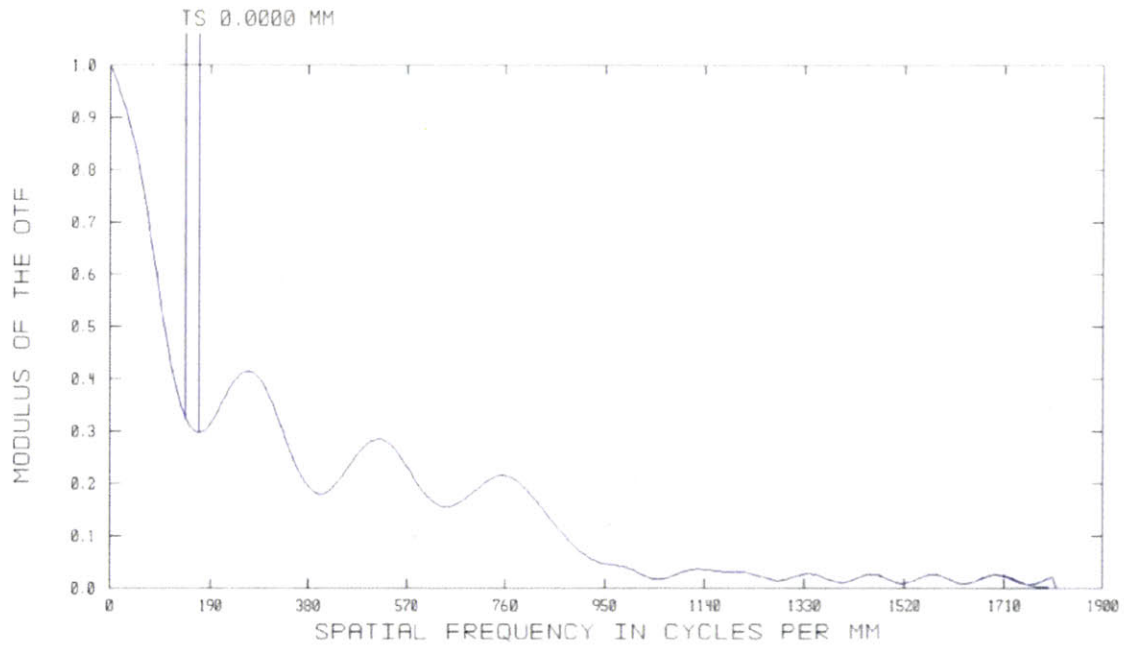
FIGURE 4.2: Simulated modulation transfer function for a real bilaterally-telecentric system comprised of two cylindrical singlet lenses with $f_1 = 250$ mm and $f_2 = 50$ mm. Note that this system (implemented in ZEMAX) is representative of the real imaging system used here in experimentation and yields modulation transfer of between 20% and 30% at the spatial frequencies of interest (roughly between 333 line pairs per mm and 500 line pairs per mm, corresponding to imaged feature sizes between 1.5 μm and 1 μm.

is described in Section 4.2.2.

The read-out process by which the exposed photorefractive polymer diffracts light into a desired distribution is described in Section 4.2.3. Simulated results from the read-out model are given in Section 4.2.4.

4.2.1 Micro-Optical Field Generation for PRP Exposure

Modeling of the evolution of the field arriving at the photorefractive polymer is accomplished as follows:

1. The light incident on the SLM (*i.e.*, emerging from the beam-expanding optics) is modeled as a monochromatic plane wave. The SLM modulates the plane wave in amplitude only with the fringe pattern.

2. The modulated beam that is incident at the entrance pupil of the telecentric imaging system is modeled via a free-space propagation integral relating it to the modulated field at the SLM.

3. The telecentric imaging system is modeled in both an *ideal* configuration and its *real* configuration as implemented in the experiments. In the ideal configuration, the imaging system is described by a phase transformation for the first lens, free-space propagation to the second lens, and a phase transformation for the second lens. In the real configuration, the imaging system is described by its point spread function (as calculated in ZEMAX and depicted in the previous section).

4. In both cases considered for the imaging system, the field arriving at the photorefractive polymer is found via free-space propagation from the exit pupil to the photorefractive polymer.

These steps are detailed in the following sections.

4.2.1.1 Spatial Modulation of Plane Wave and Free-Space Propagation

The illumination of the SLM with collimated, monochromatic light is modeled as amplitude modulation of a coherent electric field representing a monochromatic plane wave as $U_M(x,y) = A_{SLM}(x,y)U_0 e^{j2\pi\phi_0/\lambda}$, where $U_M(x,y)$ is the modulated field, $A_{SLM}(x,y)$ is the SLM modulation pattern, U_0 is the plane wave amplitude, ϕ_0 is random initial phase of the plane wave, and λ is the illumination wavelength. For the current study, an infinite test 1-D diffraction grating is employed as the SLM pattern; this grating can be expressed as $A_{SLM}(x,y) = \sum_{n=-\infty}^{\infty} \Pi\left(\frac{x-n\Lambda}{\frac{\Lambda}{2}}\right)$, where $\Pi(\cdot)$ is the rectangle function, Λ is the grating period, and n is the grating finger index.

The modulated field $U_M(x,y)$ is then described after propagation to the front lens plane

a distance z away from the SLM via the convolution form of the Fresnel diffraction integral,

$$U_{FL}(x,y) = \frac{e^{jkz}}{j\lambda z} \int_{-\infty}^{\infty} \int_{-\infty}^{\infty} U_M(\xi,\eta) \, e^{\frac{jk}{2z}[(x-\xi)^2+(y-\eta)^2]}]d\xi d\eta \qquad (4.1)$$

where $U_{FL}(x,y)$ is the field at the front lens plane, (x,y) are the spatial coordinates at the front lens plane, $k = 2\pi/\lambda$ is the wavenumber, and (ξ, η) are the spatial coordinates at the plane of the SLM [3, 16]. Note the diffraction geometry used in this formulation is the same as that depicted in Fig. 1.5. Fresnel propagation is implemented in computer via 2-D fast Fourier transformation and MATLAB code is given in Appendix B, Section B.1.

4.2.1.2 Bilaterally-Telecentric Imaging System with Ideal Thin Cylindrical Lenses

In the ideal case, the evolution of the field U_{FL} arriving at the entrance pupil of the telecentric imaging system through that system is found by means of phase transformation, in which the lenses are treated as phase-only transformation elements [3]. The phase transformation transmissive function for an ideal singlet cylindrical lens is described by $t(x,y) = L(x,y)e^{-\frac{jk}{2f}x^2}$, where $L(x,y)$ is the two-dimensional (binary) aperture function for the cylindrical lens, $k = 2\pi/\lambda$ is the magnitude of the optical wavevector of the incident beam, λ is the optical wavelength, and f is the focal length.

The modeling scheme for the ideal telecentric system is depicted in Fig. 4.3. To model the effect of the overall imaging system, the field $U_{FL}(x,y)$ arriving at the entrance pupil is first multiplied by the phase transformation transmissive function $t_1(x,y) = e^{-\frac{jk}{2f_1}x^2}$ representing the first lens, then the transformed field $U_{FL'}(x,y) = U_{FL}(x,y)t_1(x,y)$ is described after propagation to the next successive lens element by Fresnel diffraction over a distance $z_1 = f_1 + f_2$ as above to yield the field arriving at the second lens $U_{BL}(x',y')$. The next phase transformation transmissive function $t_2(x,y) = e^{-\frac{jk}{2f_2}x'^2}$ is applied to that field to yield the field $U'_{BL}(x',y') = U_{BL}(x',y')t_2(x',y')$ at the exit pupil of the imaging system. The field $U_{PR}(x'',y'')$ arriving at the photorefractive polymer is again found via Fresnel diffraction over a distance z_2.

The MATLAB code for this process is given in Appendix B, Section B.2.

4.2.1.3 Bilaterally-Telecentric Imaging System with Real Cylindrical Lenses

The modeling scheme for the "real" telecentric system case is depicted in Fig. 4.4. In the real telecentric system case, the field U_{FL} arriving at the entrance pupil of the telecentric imaging system is transformed by that system by means of convolution with its point spread function to yield the field U_{PR} emerging at the exit pupil as $U_{PR}(x,y) = U_{FL}(x,y) * h(x,y)$, where $h(x,y)$ is the point spread function of the imaging system, calculated in ZEMAX and $*$ is the convolution operator. Note that the PSF is calculated only for solving for the field
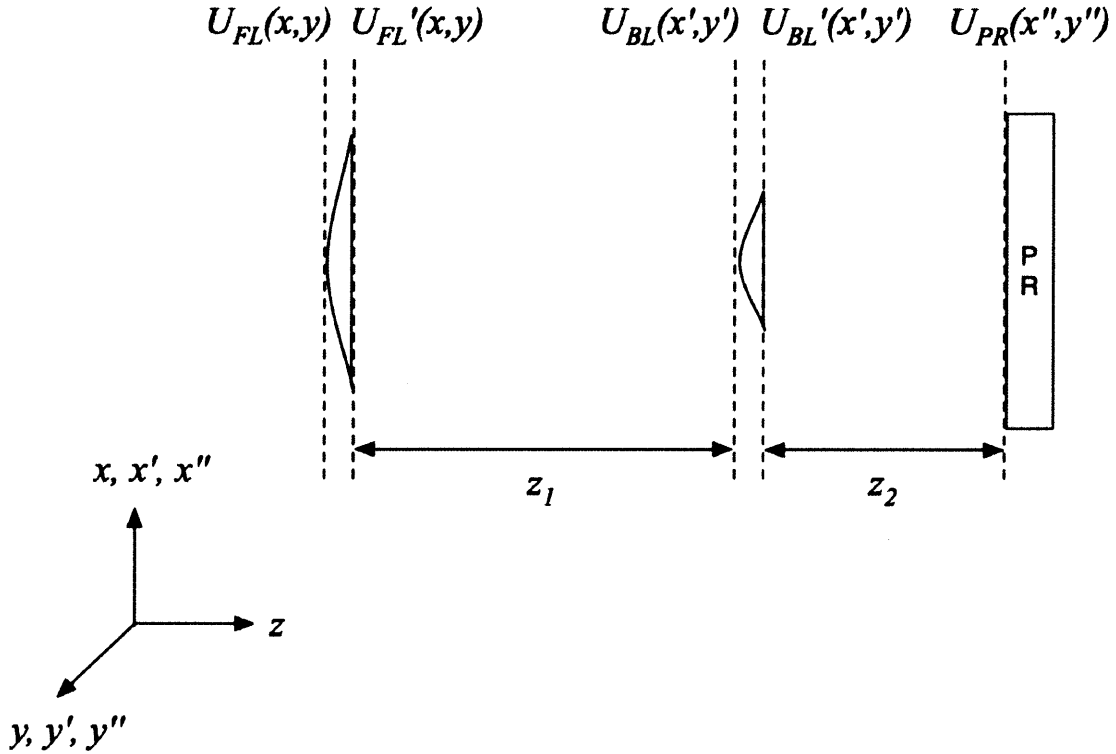
FIGURE 4.3: Field coordinates and modeling scheme for an ideal telecentric imaging system. Both lenses are modeled as ideal thin cylindrical lenses with complex phase transformation functions given by $t_1(x,y) = e^{-\frac{jk}{2f_1}x^2}$ and $t_2(x',y') = e^{-\frac{jk}{2f_2}x'^2}$. Note that this depiction is a "top-view" of the system and the lenses only have curvature in the $\hat{x}$ direction. $U_{FL}(x,y)$ is the field corresponding to the spatially-modulated plane wave arriving at the entrance pupil of the telecentric system, $U'_{FL}(x,y) = U_{FL}(x,y)t_1(x,y)$ is the first phase-transformed field, $U_{BL}(x',y')$ is the field arriving at the second lens, $U'_{BL}(x',y') = U_{BL}(x',y')t_2(x',y')$ is the second phase-transformed field, and $U_{PR}(x'',y'')$ is the field arriving at the photorefractive polymer.
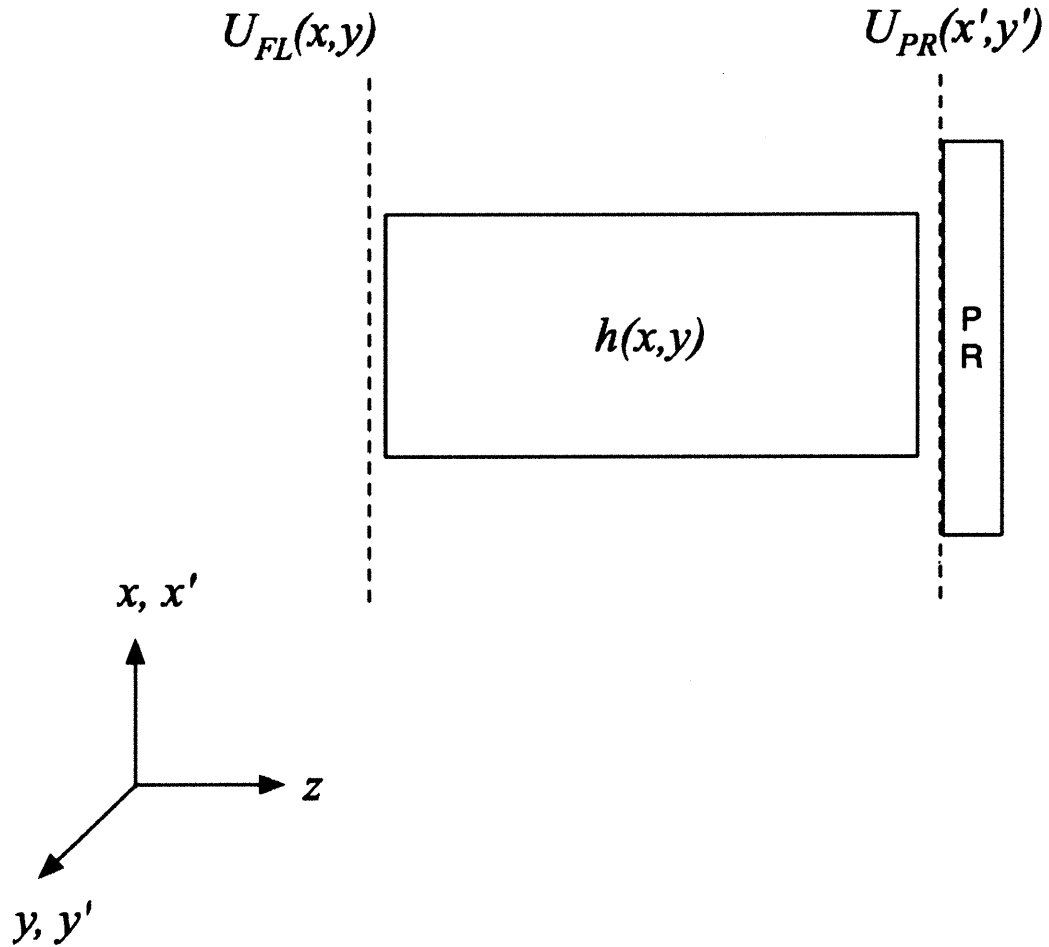
FIGURE 4.4: Field coordinates and modeling scheme for the real telecentric imaging system. The lenses and free-space distances in the system are collectively modeled by the system's point spread function $h(x, y)$, which is calculated in ZEMAX. $U_{FL}(x, y)$ is the field corresponding to the spatially-modulated plane wave arriving at the entrance pupil of the telecentric system, $U_{BL}(x, y) = U_{FL}(x, y) * h(x, y)$ is the field emerging from the exit pupil of the telecentric system, and $U_{PR}(x', y')$ is the field arriving at the photorefractive polymer.

arriving at the front face of the photorefractive polymer and *not* for any points within its volume. For this method, note that there is a coordinate shift to relate the spatial coordinates (x, y) at the lens plane to the spatial coordinates (x', y') at the plane of the photorefractive polymer as $(x', y') = (Mx, My)$, where $M = 1/5$ is the de-magnification.

The MATLAB code for this process is given in Appendix B, Section B.3.

4.2.2 Photorefractive Polymer Exposure

The field $U_{PR}(x, y, z)$ arriving at all points within the volume of the photopolymer is calculated in discrete "steps" along the propagation direction $\hat{z}$ using Fresnel diffraction for a range of propagation distances $z \in [z_0, z_0 + T]$, where z_0 is the distance from the exit pupil of the imaging system to the front plane of the recording medium and T is the thickness of the recording medium. Note that for this model, the normal of the recording medium is oriented parallel to the optical axis (*i.e.*, no slanted geometry).

The incident intensity $(I(x, y, z) = |U_{PR}(x, y, z)|^2)$ in the volume of the photorefractive polymer is converted to a phase volume hologram by means of refractive index modulation, modeled as $\Delta n(x, y, z) = \alpha t |U_{PR}(x, y, z)|^2$, where α is a constant for the material describing the strength of the photorefractive modulation and t is exposure time [15,39,40].

The MATLAB code for this process is given in Appendix B, Section B.4.

4.2.3 Diffracted Image Readout Model

Simulation of the diffracted readout from the recorded volume phase hologram is accomplished via the Alferness *thin-grating decomposition method* (TGDM), in which the volume phase modulation is treated as as a discrete number N of infinitely-thin phase-only gratings that are separated by a thickness $\Delta z = T/(N - 1)$, where T is the thickness of the volume hologram [39,41,42]. For validity of this method, the number of thin gratings for the decomposition N should be chosen such that Δz allows for the Kogelnik thickness factor ("Q") to be on the order of one; for a generalized thick grating with a single dominant spatial frequency, $Q = 2\pi\lambda\Delta z/\Lambda^2$, where λ is the optical read-out wavelength and Λ is the grating period [43]. Therefore, N should be chosen such that $N \approx \lceil 2\pi\lambda T/\Lambda^2 + 1 \rceil$. The regions between the thin gratings have constant (*i.e.*, unmodulated) refractive indices. The implemented algorithm can be summarized as follows:

1. The recorded refractive index distribution in the volume hologram $\Delta n(x, y, z)$ is converted into a series of N thin gratings equally spaced in $\hat{z}$ by Δz such that $N \approx \lceil 2\pi\lambda T/\Lambda^2 + 1 \rceil$ and $\Delta z = T/(N - 1)$. The complex transmittance (*i.e.*, phase transformation) of the ith thin grating is given by $t_i(x, y) = e^{j2\pi\Delta n(x,y,z=(i-1)\Delta z)\Delta z}$, where $i \in [1, N]$.

2. The read-out field incident on the recording medium $U_R(x, y, z = z_0)$ is transformed by the first thin grating to yield the field immediately after transformation, *i.e.*, $U_1^+(x, y, z = z_0) = t_1(x, y)U_{PR}(x, y, z = z_0)$.

3. The field then incident on the second thin grating, *i.e.*, $U_2^-(x, y, z = z_0 + \Delta z)$ is found via Fresnel diffraction as:

$$U_2^-(x, y, z = z_0 + \Delta z) = \frac{e^{jk\Delta z}}{j\lambda\Delta z} \int_{-\infty}^{\infty} \int_{-\infty}^{\infty} U_1^+(\xi, \eta, z = z_0) e^{\frac{jk}{2\Delta z}[(x-\xi)^2 + (y-\eta)^2]} d\xi d\eta$$

(4.2)

where (ξ, η) are spatial coordinates in the plane of the first thin grating and (x, y) are spatial coordinates in the plane of the second thin grating.

4. The field incident on the second thin grating $U_2^-(x, y, z = z_0 + \Delta z)$ is transformed by the second thin grating to yield the field immediately after transformation, *i.e.*, $U_2^+(x, y, z = z_0 + \Delta z) = t_2(x, y)U_2^-(x, y, z = z_0 + \Delta z)$.

5. Steps 3 (propagation step) and 4 (transformation step) are repeated for all $i \in [1, N]$, with z incrementing by Δz for each iteration (*i.e.*, $z = z_0 + (i - 1)\Delta z$) to find the field emerging from the Nth thin grating.

6. Finally, the field $U_{D0}(x, y, z = z_0 + N\Delta z)$ emerging from the photorefractive polymer is found by a final Fresnel diffraction step over a distance Δz. Then, the field at any arbitrary screen location z_S from the exit face of the photorefractive polymer can be found via a subsequent Fresnel diffraction step.

The MATLAB code for this process is given in Appendix B, Section B.5.

4.2.4 Illumination Scheme

Diffracted read-out is modeled via thin-grating decomposition as detailed above; in the current model, the input to the TGDM algorithm is a field representative of a Gaussian beam at $\lambda = 632.8$ nm. This is analogous to probing a recorded diffraction grating in the photorefractive polymer with an unmodified beam from a Helium-Neon laser at $\lambda = 632.8$ nm. The field from the laser is given by the Gaussian beam expression,

$$U_R(x, y) = \sqrt{\frac{2P_0}{\pi w_0^2}} \cdot e^{-\left(\frac{x^2 + y^2}{w_0^2}\right)}$$

(4.3)

where P_0 is the beam power and w_0 is the beam waist size (which is related to the full-width at half-maximum divergence angle of the beam as $w_0 = \lambda/(\pi\theta_{FWHM}/1.18)$, where θ_{FWHM} is the full-width at half-maximum divergence angle in radians) [44].

4.2.5 Wave Optics Model Parameters & Results

Numerical parameters used for the optical modeling scheme are listed in Table 4.1.

The simulated diffracted irradiance distributions emerging from the simulated exposure of the photorefractive polymer (according to the method in Section 4.2.2) via direct fringe

TABLE 4.1: Parameters used in optical modeling of direct fringe writing.

Writing Wavelength	532 nm
Writing Power	200 mW
SLM Grating Pitch	17 μm
Ideal Lens 1 Focal Length	250 mm
Ideal Lens 2 Focal Length	50 mm
Photorefractive Material Thickness	100 mm
Number of "Thin" Gratings	30
Exposure Time	10 s
α Constant	10^{-1}
Read-out Wavelength	632.8 nm
Read-out Power	20 mW
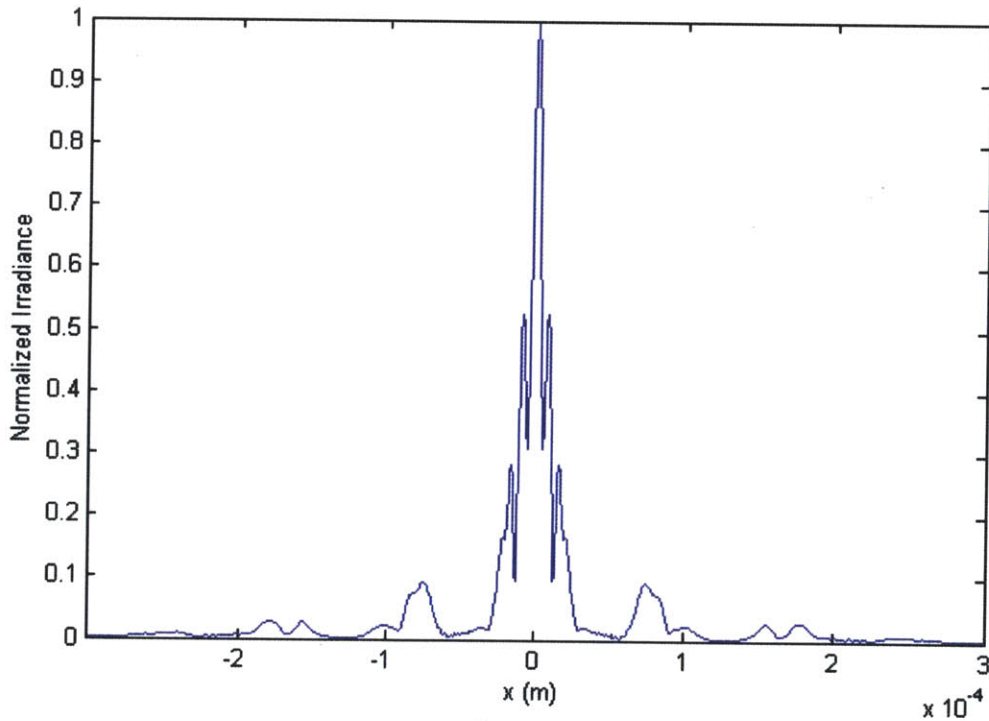
FIGURE 4.5: Normalized diffracted irradiance distribution from volume phase hologram exposed in photorefractive polymer via simulated direct fringe writing of a 1-D diffraction grating pattern via an "ideal" telecentric imaging system. This distribution appears at a screen 300 μm from the exit face of the recording medium. The -1 and $+1$ diffracted orders are seen to the left and right of the main lobe at the origin. Note that the spacing of the side lobes indicates a first-order diffracted angle of roughly 13°, which corresponds to a grating period of roughly 3 μm. This is consistent with the period of the original diffraction grating and the nominal de-magnification.
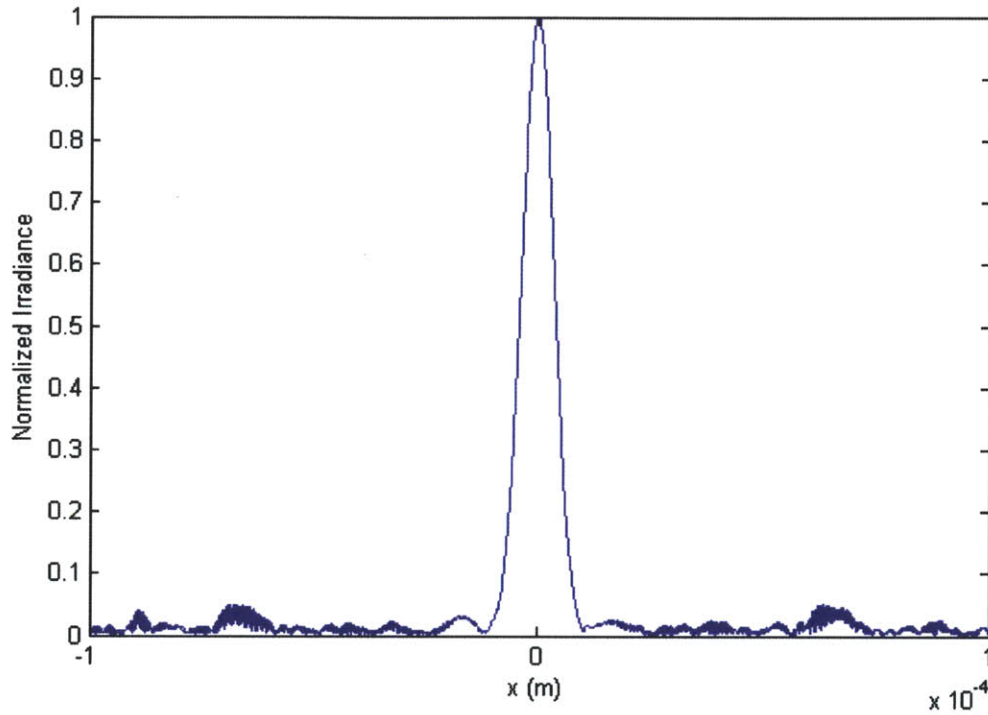
FIGURE 4.6: Normalized diffracted irradiance distribution from volume phase hologram exposed in photorefractive polymer via simulated direct fringe writing of a 1-D diffraction grating pattern via a model of the real experimental telecentric imaging system. This distribution appears at a screen 300 μm from the exit face of the recording medium. The -1 and $+1$ diffracted orders are seen to the left and right of the main lobe at the origin. The -1 and $+1$ diffracted orders are seen to the left and right of the main lobe at the origin. Note that the spacing of the side lobes indicates a first-order diffracted angle of roughly 13°, which corresponds to a grating period of roughly 3 μm. This is consistent with the period of the original diffraction grating and the nominal de-magnification.

writing (according to the methods in Section 4.2.1) with this probe beam are depicted in Fig. 4.5 (for direct writing via an ideal bilaterally-telecentric imaging system) and Fig. 4.6 (for direct writing via a representation of the real bilaterally-telecentric imaging system used in experimentation).

The diffraction efficiency is calculated by finding the power contained in each of the -1st, 0th, and $+1$st diffraction orders. The following equation relates irradiance incident on a spatial area to power:

$$P_A = \frac{c\epsilon_0}{2} \iint_A |U(x,y)|^2 \, dx \, dy \tag{4.4}$$

where c is the speed of light in vacuum, ϵ_0 is the permittivity of free space, and A represents the area over which the incident power should be calculated. Diffraction efficiency can then be calculated as $\eta_D = P_A/P_0$, where P_A is the power incident in the area corresponding to a particular diffracted order and P_0 is the power incident on the recording medium (photorefractive polymer) from the read-out probe beam. From the irradiance distributions depicted in Fig. 4.5 and Fig. 4.6, the 1st order diffraction efficiencies are calculated to be 7% for the case of the ideal bilaterally-telecentric system and 1% for the case of the real bilaterally-telecentric system.

4.3 Observations

The simulated modulation transfer function of the experimental bilaterally-telecentric imaging system indicates a modulation transfer between 20% and 30% at the spatial frequencies of interest; this performance does not yield *ideal* imaged contrast but may yield *sufficient* imaged contrast. In the existing interference-based photorefractive holographic imager, reference-to-object beam ratios of up to 5-to-1 are employed; the maximal contrast in the fringes generated by interference is similarly limited by the beam ratio. Although a modulation transfer of 20% in the imaging system is not sufficiently high to be considered highly resolving by many definitions, it may suffice for the purposes of fringe imaging considering the beam ratios (and thereby lower fringe pattern contrasts) employed successfully in many interference-based holographic imagers.

Results from the wave optics model do indicate that direct fringe imaging of diffraction gratings does yield the diffraction somewhat consistent with that expected from a diffraction grating of lower pitch. The result depicted in Fig. 4.5 indicates a 1st order diffracted angle of 13°; this is consistent with the pitch of the input grating and the nominal demagnification applied. The diffraction efficiencies that have been computed are not wholly representative of real-world performance, for reasons depicted in the next section.

4.4 Limitations of Current Modeling & Simulation Approach

The modeling approach described here does not completely describe all factors related to direct fringe writing in the photorefractive material. Several factors not included are itemized

here:

- *Field polarization.* Polarization is neglected in this model although it plays a role in the LCoS device's spatial modulation and in the recording and read-out dynamics and mechanisms in the photorefractive material. A more complete model should trace polarization states through the system and assimilate the effects of the optical components and recording medium on these polarization states.

- *Microstructure of spatial light modulator.* The pixel microstructure (*i.e.*, pixel fill factor) of the spatial light modulator is neglected in this model although it creates significant (and undesirable) diffractive effects in the actual system. A more complete model should include the effect of the pixel microstructure on the micro-optical field arriving at the photorefractive polymer.

- *Contrast limitations of spatial light modulator.* The spatial light modulator has an inherent maximal contrast and therefore imposes its own modulation transfer function on the fringe patterns it displays. The current model only takes into account the effect of the MTF of the imaging system but a more complete model should account for the MTF of the SLM as well.

- *Cross-polarization scheme for amplitude modulation read-out; Malus' law.* The LCoS device used in the cross-polarizer configuration for the experiments described here effectively reads out amplitude modulation from states of polarization rotation. This behavior is typically governed by Malus' law (*i.e.*, $I = I_0 \cos^2 \theta$, where I is the output intensity, I_0 is the incident intensity, and θ is the angle between the polarization direction of the incident light and the polarizer's axis) and should be included in a more complete model.

- *Slanted geometry of photorefractive polymer.* This model assumes that the normal of the photorefractive polymer surface is oriented in parallel with the writing beam and that therefore the grating vector of the written fringes is concurrent with the axis of the material. In a more complete model (and to fully depict the experimental conditions, in which the photorefractive material is slanted obliquely relative to the writing beam), arbitrary writing and fringe geometries should be supported.

- *Orientational photorefractivity, diffusion and trapping, and electro-optic effects in photorefractive material.* The current model uses a simple exposure model in which the refractive index modulation is merely related to incident intensity and exposure time. However, this relationship does not capture the effect of orientationally-enhanced photorefractivity nor does it adequately describe the electro-optically induced charge diffusion and trapping mechanisms that form the phase grating. These factors need to be included in a more complete model.

- *Direct writing of holographic fringe patterns corresponding to 3-D images.* The current model uses test grating patterns to investigate direct fringe writing. While useful as a validation exercise, further insights into factors affecting system performance can

likely be gained by using fringe patterns corresponding to 3-D images, and especially those computed using the RIP and DSCP algorithms and used for experimentation.

Chapter 5

Experimental Results & Observations

At the time of this writing, a testbed for direct fringe writing experiments with the photorefractive polymer has been built-up and preliminary results have been gathered. These results and some observations are presented here.

5.1 Validation Results

For validation of the experimental direct fringe writing testbed, the simplest test case is a 1-D diffraction grating; therefore, this validation of the premise of direct writing of fringe patterns was accomplished with test gratings. The initial experiment involved a "contact" printing method, in which a single beam was passed through a transmissive diffraction grating that was placed in contact with the photorefractive polymer. The second experiment involved the use of the optical setup detailed in Section 3.3, with a diffraction grating pattern displayed on the spatial light modulator.

5.1.1 "Contact" Printing of 1-D Diffraction Grating Patterns

In the "contact" printing experiment, a ruled diffraction grating with $\Lambda = 1.9 \ \mu$m was placed in contact with the photorefractive polymer. A single beam at $\lambda = 532$ nm was passed through the grating and photorefractive polymer and thereby the "shadow" of the diffraction grating was used to expose the material. The writing beam was set to an output power of 300 mW and was incident upon the grating and photorefractive polymer at an oblique slant angle of 45° (within the slant angle range necessary for the orientationally-enhanced photorefractive effect) for an exposure time of 30 s. For read-out of the exposure, a beam with the same characteristics as the writing beam except a reduced power of 10 mW was used. The diffraction from this probing is depicted in Fig. 5.1.

This result shows clear diffraction orders, identical in spread to those that would arise from probing the original (removed) diffraction grating. For this experiment, a peak 1st order diffraction efficiency of 6% from the probed grating in the photorefractive polymer was observed. This result affirmed base viability of direct fringe writing and motivated the further inquiry presented here.
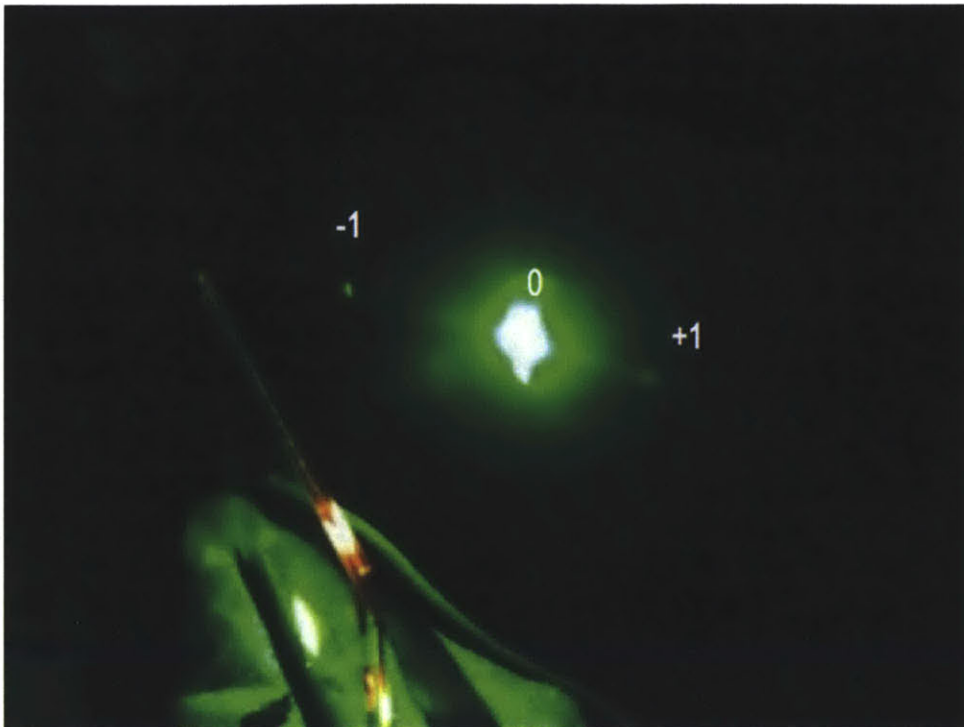
FIGURE 5.1: Photograph of the diffraction from a "contact" printed diffraction grating, showing clear diffraction orders resulting from a sinusoidal grating.

5.1.2 Direct Writing of 1-D Diffraction Grating Patterns from SLM

For validation of the direct fringe writing approach presented in Section 3.3, a 1-D binary grating was displayed on the SLM and directly written into the photorefractive polymer. For this test case, the grating had an overall resolution identical to that of the SLM and so no spatial multiplexing was needed. The writing parameters and observed results from this test are listed in Table 5.1. The written grating was probed with an illumination beam from a helium-neon laser at $\lambda = 632.8$ nm and p-polarization; the resulting diffraction is pictured in Fig. 5.2. Note that the observed grating half-pitch listed in Table 5.1 was back-calculated from the simple grating equation ($\sin\theta_m = m\lambda/\Lambda - \sin\theta_i$, where θ_m is the diffracted angle of the mth diffracted order, m is the diffracted order index, λ is the probing wavelength, Λ is the grating pitch, and θ_i is the angle of incidence of the probe beam relative to the normal vector of the written diffraction grating).

This result shows clear diffraction orders resulting from a sinusoidal 1-D grating in the photorefractive polymer. Because only the -1 and $+1$ diffracted orders were observed, it can be deduced that the high spatial frequency content corresponding to the "hard" edges of the displayed binary grating on the SLM were effectively cutoff by low-pass filtering by the imaging system. The observed first-order diffraction efficiency of 8% is an indicator of reasonable performance.

TABLE 5.1: Writing parameters for and observations for directly-written diffraction grating in photorefractive polymer.

PR Polymer Bias Voltage	5.0 kV
Grating Fringe Pattern Resolution	1920 x 1080
Grating Half-Pitch	8.5 μm
Irradiance	0.75 W/cm^2
Exposure Time	10 s
Observed Grating Half-Pitch	2.5 μm
Observed Diffraction Efficiency	8%
Estimated Grating Persistence	300 s
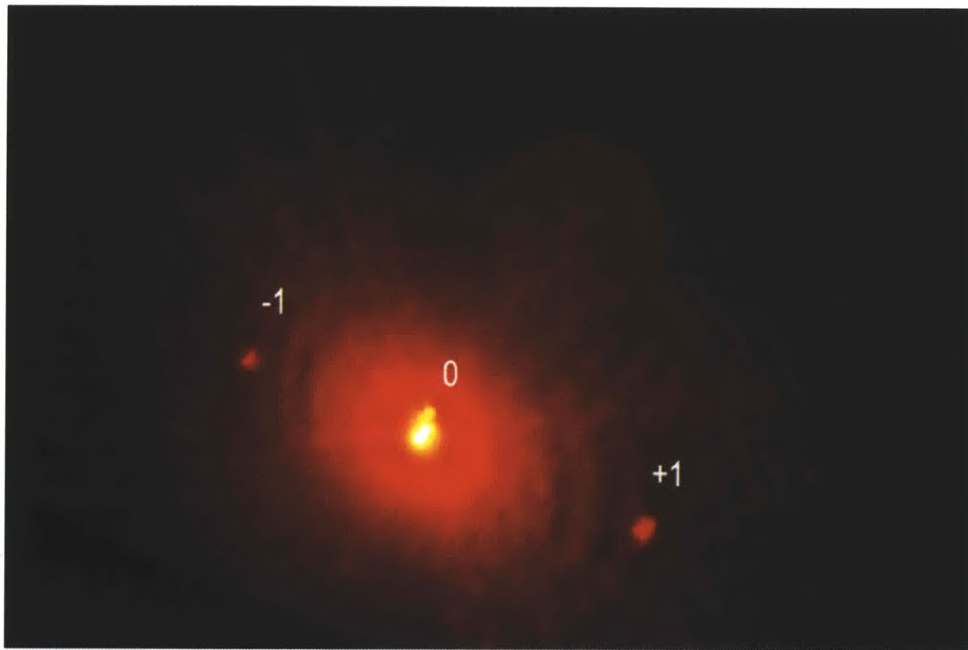
FIGURE 5.2: Photograph of the diffraction from an imaged diffraction grating, showing clear diffraction orders resulting from a sinusoidal grating.

5.2 Direct Fringe Writing of Holographic Fringes Computed with the RIP Algorithm

Initial validation tests of the system with fringe patterns corresponding to 3-D images were carried out using fringes computed with the RIP algorithm. A computer graphics model of a teacup (depicted in Fig. 5.3) was used as input for RIP holographic fringe computation. Writing parameters and persistence observations are detailed in Table 5.2. The resulting image in the photorefractive material due to the direct fringe writing of these computed

TABLE 5.2: Writing parameters and observations for directly-written HPO teacup fringes computed via RIP algorithm.

PR Polymer Bias Voltage	5.0 kV
Overall Fringe Pattern Resolution	48000 x 1080
Exposure Time per Elemental	10 s
Maximum Irradiance per Elemental	1.25 W/cm^2
Total Writing Time	300 s
Estimated Persistence per Elemental	300 s
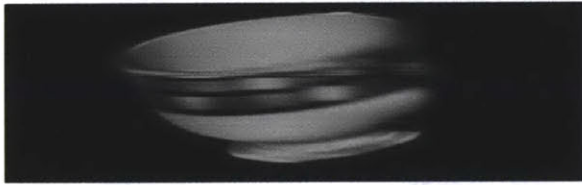
FIGURE 5.3: Teacup model used for RIP stereogram fringe generation.
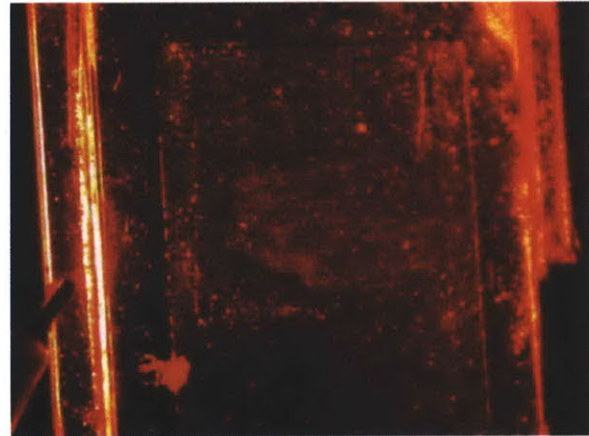
FIGURE 5.4: Resulting image of teacup model in photorefractive material.

fringes is shown in Fig. 5.4.

5.3 Direct Fringe Writing of Holographic Fringes Computed with the DSCP Algorithm

TABLE 5.3: Writing parameters and observations for directly-written HPO Stanford Bunny diffraction specific coherent panoramagram in photorefractive polymer.

PR Polymer Bias Voltage	5.0 kV
Overall Fringe Pattern Resolution	51840 x 1080
Exposure Time per Elemental	10 s
Maximum Irradiance per Elemental	1.25 W/cm^2
Total Writing Time	350 s
Estimated Persistence per Elemental	300 s

FIGURE 5.5: Stanford Bunny model used for DSCP fringe generation.
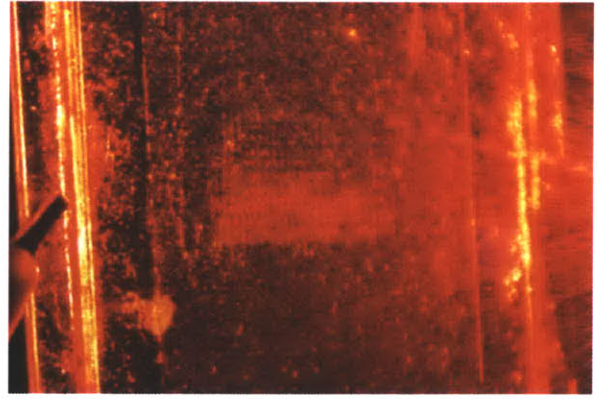
FIGURE 5.6: Resulting holographic image of Stanford Bunny model.

Tests of the system with fringe patterns computed using the DSCP algorithm were carried out using a model of the Stanford Bunny for test imagery (depicted in Fig. 5.5). Writing parameters and persistence observations are detailed in Table 5.3. The resulting holographic image in the PR material due to the direct fringe writing of these computed fringes is shown in Fig. 5.6.

5.4 Observations

The current results do indicate that diffraction gratings can be written in the photorefractive polymer via single-beam direct fringe writing. Furthermore, the demonstration of direct writing of holographic fringes corresponding to 3-D images indicates some degree of feasibility for the approach. Clearly, there remains much room for improvement of the display quality. At the present time, diffraction efficiency of the resulting images is poor and the images suffer from low contrast, low discriminability, and low persistence – all of which pose problems for direct viewing. These issues are discussed in further detail in Chapter 6.

Chapter 6

Future Work & Extensions

Direct fringe writing offers several advantages for a photorefractive holographic imager; at the time of this writing, a testbed for experiments in direct fringe writing has been built-up and preliminary results reflecting on the efficacy of some of the strategies in system design have been gathered. However, there remains much room for performance improvement and experimentation with strategies for direct fringe writing that are outside the scope of this thesis. Furthermore, several applications that are well-suited to a photorefractive holographic imager merit exploration. Future work that is a direct extension of the work contained in this thesis as well as other possible extensions are explored here.

6.1 Improvement of Recording Process

The current recording setup has some drawbacks that adversely affect ultimate display performance:

- *Cross-polarization scheme for LCoS amplitude readout.* Using two crossed polarizers may not yield the maximum output contrast possible for amplitude modulation with the LCoS device. Furthermore, laminated film polarizers are easily susceptible to optical damage at high incident irradiance levels. A different scheme for amplitude modulation read-out (*e.g.*, a cube beamsplitter) should be employed in future iterations.

- *Non-uniform writing beam distribution.* The writing beam that is incident on the SLM for modulation is currently an expanded and collimated Gaussian beam originating from a DPSS laser. The Gaussian irradiance profile may not be ideal for direct fringe writing and a more uniform distribution may be preferable. A diffusing beam homogenizer can be added to the optical setup to enable this.

6.2 Improvement of Read-out Process (Illumination Setup)

The current readout setup has some drawbacks that adversely affect the image quality perceived by a viewer:

- *Laser illumination creates speckle.* The illumination of the recorded fringe patterns with laser light produces speckle which can lower perceived image quality. This can be alleviated by using a high-powered LED light source in lieu of a laser.

- *Laser illumination creates spurious interferograms on glass surface.* The interference of the laser light with itself (due to the multiple reflections between the glass layers) creates spurious intereferograms on the glass surface which distract from and lower contrast of the holographic image. This can be alleviated by using a high-powered LED light source in lieu of a laser.

- *Reflections of laser illumination from glass surface lower contrast.* The reflections of the laser light from the glass surfaces of the photorefractive polymer assembly act to lower contrast and "wash-out" the already hard-to-discriminate holographic image. This can possibly be alleviated by using an LED light source.

6.3 Improvement of Generalized Display Performance

In order to make direct fringe writing more practicable as a replacement for interference-based stereogram recording schemes, future work needs to address several performance issues; most critically, these are diffraction efficiency (image brightness), image persistence, and image discriminability.

6.3.1 Diffraction Efficiency

Diffraction efficiency is linked to a number of factors, including fringe visibility (*i.e.*, modulation efficiency or contrast in the resulting refractive index distribution from recording), exposing parameters (*e.g.*, incident irradiance and exposure time), and applied electric field strength during read-out. Improvements are likely with improvement of the imaging system MTF (up to the maximal spatial frequency indicated by its demagnification), further optimization of exposing parameters, and further characterization and optimization of the effect of the applied bias voltage.

Improvements in the imaging system are likely to result from using well-characterized spherical telescopes with good resolving power at high spatial frequencies in a spherical bilaterally-telecentric imaging setup in tandem with a cylindrical projection lens system at its output. These modifications will likely lead to higher imaged contrast and thereby higher diffraction efficiencies.

6.3.2 Image Persistence

Image persistence is largely a function of applied electric field strength but has also been observed to vary based on the particular sample of photorefractive material being used. At the time of this writing, substantial improvements in grating holding times have already been observed in photorefractive samples other than those used to obtain the results presented here. In addition, further improvement of image persistence may be possible via the use of

a voltage kick-off method, in which a large electric field is applied to the photorefractive polymer during writing then reduced after completion of the writing process [32].

6.3.3 Image Discriminability

Image discriminability is largely related to both diffraction efficiency and image persistence and improvements in these two areas will likely yield improvements in discriminability as well. Additionally, a more refined illumination setup, possibly involving high-power light-emitting diodes rather than lasers, can improve contrast.

6.4 Extensions

6.4.1 Direct Fringe Writing of DSCP Fringe Patterns Computed from Real Scenes
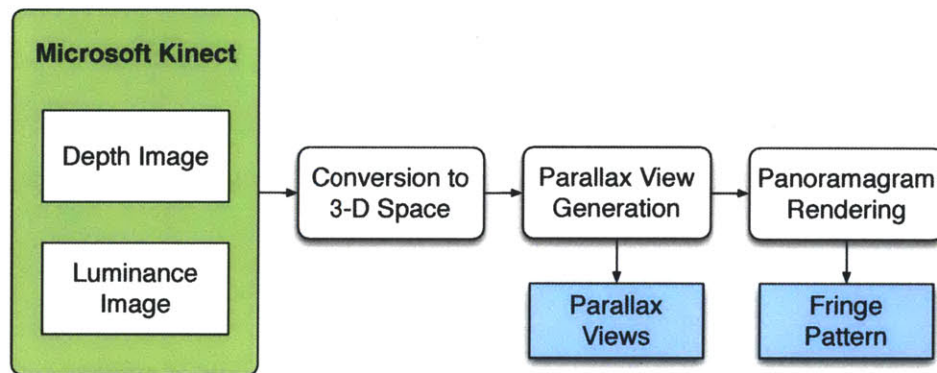
FIGURE 6.1: Pipeline for real-time generation of DSCP fringe patterns using the Microsoft Kinect peripheral.

It should be noted that while the current implementation of the DSCP fringe computation algorithm only produces "pre-rendered" fringes for recording in the photorefractive material at a later time, the algorithm can easily be integrated into the control system for real-time computation (with the caveat that such real-time computation will only be beneficial in the case of a fast writing scheme to take advantage of the fast computation). Furthermore, generation of DSCP fringe patterns corresponding to real scenes in real-time using consumer rangefinding cameras has previously been demonstrated (Fig. 6.1 depicts this process) [8]. This capability can be exploited in a future holographic telepresence scheme using a direct fringe writing approach.

6.4.2 Direct Fringe Writing for Full-Parallax Scenes

Direct fringe imaging for full-parallax images is a plausible extension but will require the adaptation of the DSCP algorithm to handle full-parallax imaging, telecentric optical imag-

73

ing using standard spherical optics, and spatial multiplexing in two dimensions.

Adaptation of the DSCP algorithm for full-parallax imaging involves using variable-rate 2-D Fresnel zone plate basis functions rather than variable-rate 1-D chirped gratings. As in the 1-D case, pre-computed Fresnel zone plate basis functions will be selected from scene depth information, the zone plates will be modulated with the intensity information of the scene, and the zone plates will be appropriately tiled to construct the composite full-parallax holographic fringe pattern.

Chapter 7

Conclusions

Direct fringe writing of computer-generated holographic fringe patterns has the potential to simplify and enhance updatable holographic imagers based around photorefractive polymers. Relative to interference-based holographic stereogram approaches, a direct fringe writing approach can allow for vastly more control over recorded hologram characteristics, simplification of system architectures, increased perceptual quality of 3-D images, and better system portability at a reduced overall system cost.

This thesis has explored several of the challenges involved with making direct fringe writing a viable alternative to the interference-based stereogram approach, including requisite imaged feature sizes and resolution issues, system architectures, and fringe computation. The experimental testbed that has been developed for direct fringe writing experiments has yielded preliminary results that indicate, with refinement of several key system parameters, direct fringe writing can possibly mitigate several of the issues associated with interference-based stereogram recording and positively enhance a photorefractive holographic imager.

It should be noted that as of the time of this writing, the author intends to continue actively working on the testbed development and on the further refinement and experimentation necessary to improve results.

Bibliography

[1] D. Gabor, "A new microscopic principle," *Nature*, vol. 161, no. 4098, pp. 777–778, 1948.

[2] P. Hariharan, *Optical Holography: Principles, Techniques, and Applications*, 2nd ed. New York, NY: Cambridge University Press, 1996.

[3] J. W. Goodman, *Introduction to Fourier Optics*, 3rd ed. Woodbury, NY: Roberts & Company, 2005.

[4] S. A. Benton and V. M. Bove, Jr., *Holographic Imaging*. Hoboken, NJ: Wiley, 2008.

[5] K. Buse and E. Kratzig, "Inorganic photorefractive materials," in *Holographic Data Storage*, Eds: H. Coufal, D. Psaltis, and G. Sincerbox. Springer, New York, 2000.

[6] B. Kippelen, "Overview of photorefractive polymers for holographic data storage," in *Holographic Data Storage*, Eds: H. Coufal, D. Psaltis, and G. Sincerbox. Springer, New York, 2000.

[7] J. T. McCrickerd and N. George, "Holographic stereogram from sequential component photographs," *Applied Physics Letters*, vol. 12, no. 1, pp. 10–12, 1968.

[8] J. Barabas, S. Jolly, D. E. Smalley, and V. M. Bove, Jr., "Diffraction Specific Coherent Panoramagrams of Real Scenes," *Proc. SPIE Practical Holography XXV*, v. 7957, 2011.

[9] D. DeBitetto, "Holographic panoramic stereograms synthesized from white light recordings," *Applied Optics*, vol. 8, 1969.

[10] M. A. Teitel, *Anamorphic raytracing for synthetic alcove holographic stereograms*, S.M. Thesis, Massachusetts Institute of Technology, 1986.

[11] M. Holzbach, *Three-dimensional image processing for synthetic holographic stereograms*, S.M. Thesis, Massachusetts Institute of Technology, 1987.

[12] G. Barbastathis and D. Psaltis, "Volume holographic multiplexing methods," in *Holographic Data Storage*, Eds: H. Coufal, D. Psaltis, and G. Sincerbox. Springer, New York, 2000.

[13] N. Peyghambarian, S. Tay, P.-A. Blanche, R. Norwood, and M. Yamamoto, "Rewritable Holographic 3D Displays," *Optics & Photonics News*, OPN, vol. 19, no. 7, pp. 22–27, 2008.

[14] U. Schnars and W. Jueptner, *Digital Holography: Digital Hologram Recording, Numerical Reconstruction, and Related Techniques*. Berlin: Springer-Verlag Berlin Heidelberg, 2005.

[15] M. Born and E. Wolf, *Principles of Optics*, 7th ed. New York, NY: Cambridge University Press, 1999.

[16] D. J. Brady, *Optical Imaging and Spectroscopy*, John Wiley & Sons, Inc., Hoboken, NJ, USA, 2008.

[17] M. Lucente, *Diffraction-Specific Fringe Computation for Electro-Holography*, Ph.D. Thesis, Massachusetts Institute of Technology, 1994.

[18] B. Upton and J. London, *Photography*, 5th. ed. New York, NY: HarperCollins Publishers, 1994.

[19] W. Plesniak, M. Halle, V. M. Bove, Jr., and J. Barabas, "Reconfigurable image projection holograms," *Optical Engineering*, 45(11), 115801, 2006.

[20] V. M. Bove, Jr., W. Plesniak, T. Quentmeyer, and J. Barabas, "Real-time holographic video images with commodity PC hardware," *Proc. SPIE Stereoscopic Displays and Applications*, vol. 5664, pp. 255–262, 2005.

[21] J. Barabas, Q. Smithwick, and V. M. Bove, Jr., "Real-time shader rendering of holographic stereograms," *Proceedings of SPIE Practical Holography XXIII: Materials and Applications*, 2009.

[22] Q. Y. J. Smithwick, J. Barabas, D. Smalley, and V. M. Bove, Jr., "Interactive Holographic Stereograms with Accommodation Cues," *Proc. SPIE Practical Holography XXIV: Materials and Applications*, 7619, 761903, 2010.

[23] H. Yoshikawa and K. Takei, "Development of a compact direct fringe printer for computer-generated holograms," *Proc. SPIE Practical Holography*, vol. 5290, no. 1, p. 114, 2004.

[24] K. Matsushima and A. Joko, "High-Resolution Printer for Fabricating Computer-Generated Display Holograms," *Journal of the Institute of Image Information and Television Engineers*, vol. 56, pp. 1989-1994, 2002.

[25] Y. Sakamoto, M. Morishima, and A. Usui, "Computer-generated holograms on a CD-R disk," *Proceedings of SPIE Practical Holography*, vol. 5290, no. 1, pp. 42–49, 2004.

[26] H. Yoshikawa and T. Yamaguchi, "Computer-generated holograms for 3D display," *Chinese Optics Letters*, vol. 7, no. 12., pp. 1079–1082, 2009.

[27] P. St-Hilaire, *Scalable optical architectures for electronic holography*, Ph.D. Thesis, Massachusetts Institute of Technology, 1994.

[28] F. S. Chen, J. T. LaMacchia, and D. B. Fraser, "Holographic storage in lithium niobate," *Applied Physics Letters*, vol. 13, no. 7, p. 223, 1968.

[29] S. S. Orlov and W. Phillips, "Hologram Fixing and Nonvolatile Storage in Photorefractive Materials," in *Holographic Data Storage*, Eds: H. Coufal, D. Psaltis, and G. Sincerbox. Springer, New York, 2000.

[30] A. Adibi, K. Buse, D. Psaltis, "Non-volatile holographic recording in doubly-doped lithium niobate," *Nature*, vol. 393, pp. 665-668, 1998.

[31] W. Moerner, S. Silence, and F. Hache, "Orientationally enhanced photorefractive effect in polymers," *Journal of the Optical Society of America B*, vol. 11, no. 2, p. 320, 1994.

[32] S. Tay, P. Blanche, R. Voorakaranam, A. V. Tunc, W. Lin, S. Rokutanda, T. Gu, D. Flores, P. Wang, G. Li, P. Saint-Hilaire, J. Thomas, R. A. Norwood, M. Yamamoto, and N. Peyghambarian, "An updatable holographic three-dimensional display," *Nature*, vol 451, pp. 694-698, 2008.

[33] P. A. Blanche, S. Tay, R. Voorakaranam, P. Saint-Hilaire, C. Christenson, T. Gu, W. Lin, D. Flores, P. Wang, M. Yamamoto, J. Thomas, R. Norwood, and N. Peyghambarian, "An Updatable Holographic Display for 3D Visualization," *Journal of Display Technology*, vol. 4, no. 4, pp. 424–430, 2008.

[34] J. Thomas, C. W. Christenson, P.-A. Blanche, M. Yamamoto, R. A. Norwood, and N. Peyghambarian, "Photoconducting Polymers for Photorefractive 3D Display Applications," *Chem. Mater.*, vol. 23, no. 3, pp. 416–429, Feb. 2011.

[35] R. A. Norwood, S. Tay, P. Wang, P.-A. Blanche, D. Flores, R. Voorakaranam, W. Lin, J. Thomas, T. Gu, P. St. Hilaire, C. Christenson, M. Yamamoto, and N. Peyghambarian, "Photorefractive Polymers for Updatable Holographic Displays," *ACS symposium in Organic Thin Films for Photonic Appliations*, ch. 6, 2010.

[36] P.-A. Blanche, A. Bablumian, R. Voorakaranam, C. Christenson, W. Lin, T. Gu, D. Flores, P. Wang, W.-Y. Hsieh, M. Kathaperumal, B. Rachwal, O. Siddiqui, J. Thomas, R. A. Norwood, M. Yamamoto, and N. Peyghambarian, "Holographic three-dimensional telepresence using large-area photorefractive polymer," *Nature*, vol. 468 (7320) pp. 80-83, 2010.

[37] C. W. Christenson, P. A. Blanche, S. Tay, R. Voorakaranam, T. Gu, W. Lin, P. Wang, M. Yamamoto, J. Thomas, R. A. Norwood, and N. Peyghambarian, "Materials for an Updatable Holographic 3D Display," *Journal of Display Technology*, vol. 6, no. 10, pp. 510–516, 2010.

[38] C. W. Christenson, C. Greenlee, B. Lynn, J. Thomas, P. A. Blanche, R. Voorakaranam, P. St. Hilaire, L. J. LaComb, Jr., R. A. Norwood, M. Yamamoto, and N. Peyghambarian, "Interdigitated coplanar electrodes for enhanced sensitivity in a photorefractive polymer," *Optics Letters*, vol. 36, no. 17, p. 3377, 2011.

[39] R. Alferness, "Analysis of optical propagation in thick holographic gratings," *Applied Physics A: Materials Science & Processing*, 1975.

[40] J. Jackson, *Classical Electrodynamics*. New York, NY: Wiley, 1999.

[41] R. Alferness, "Equivalence of the thin-grating decomposition and coupled-wave analysis of thick holographic gratings," *Optics Communications*, vol. 15, no. 2, pp. 209–212, Oct. 1975.

[42] H. Ichikawa, J. Turunen, and M. R. Taghizadeh, "Analysis of hybrid holographic gratings by thin-grating decomposition method," *Journal of the Optical Society of America A*, vol. 10, no. 6, pp. 1176–1183, 1993.

[43] H. Kogelnik, "Coupled wave theory for thick hologram gratings," *The Bell System Technical Journal*, 1969.

[44] O. Svelto, *Principles of Lasers*, 4th ed. New York, NY: Springer, 2009.

Appendix A

LabVIEW Virtual Instrument Block Diagram

This is the complete LabVIEW block diagram for the implemented fringe printing Virtual Instrument.
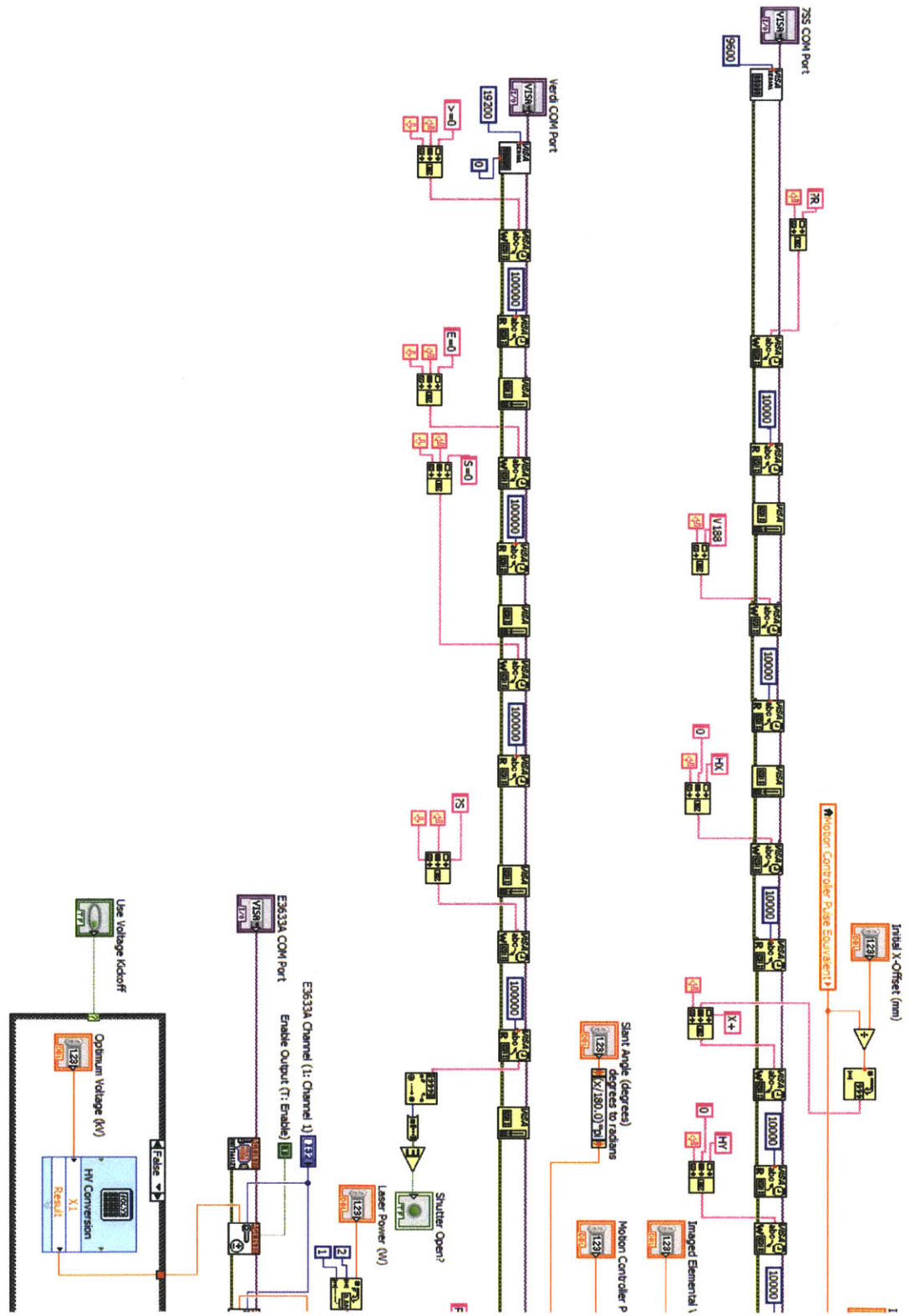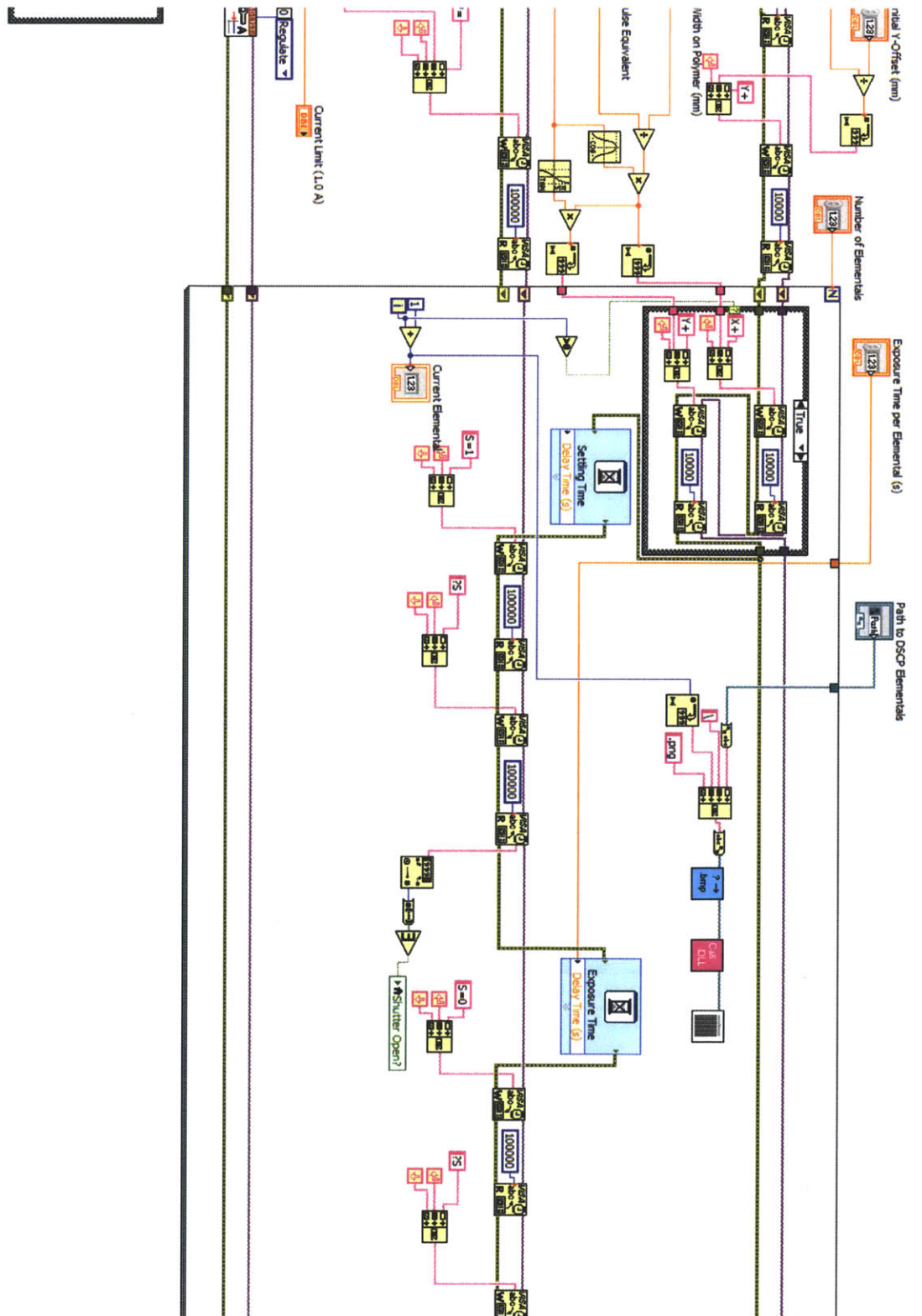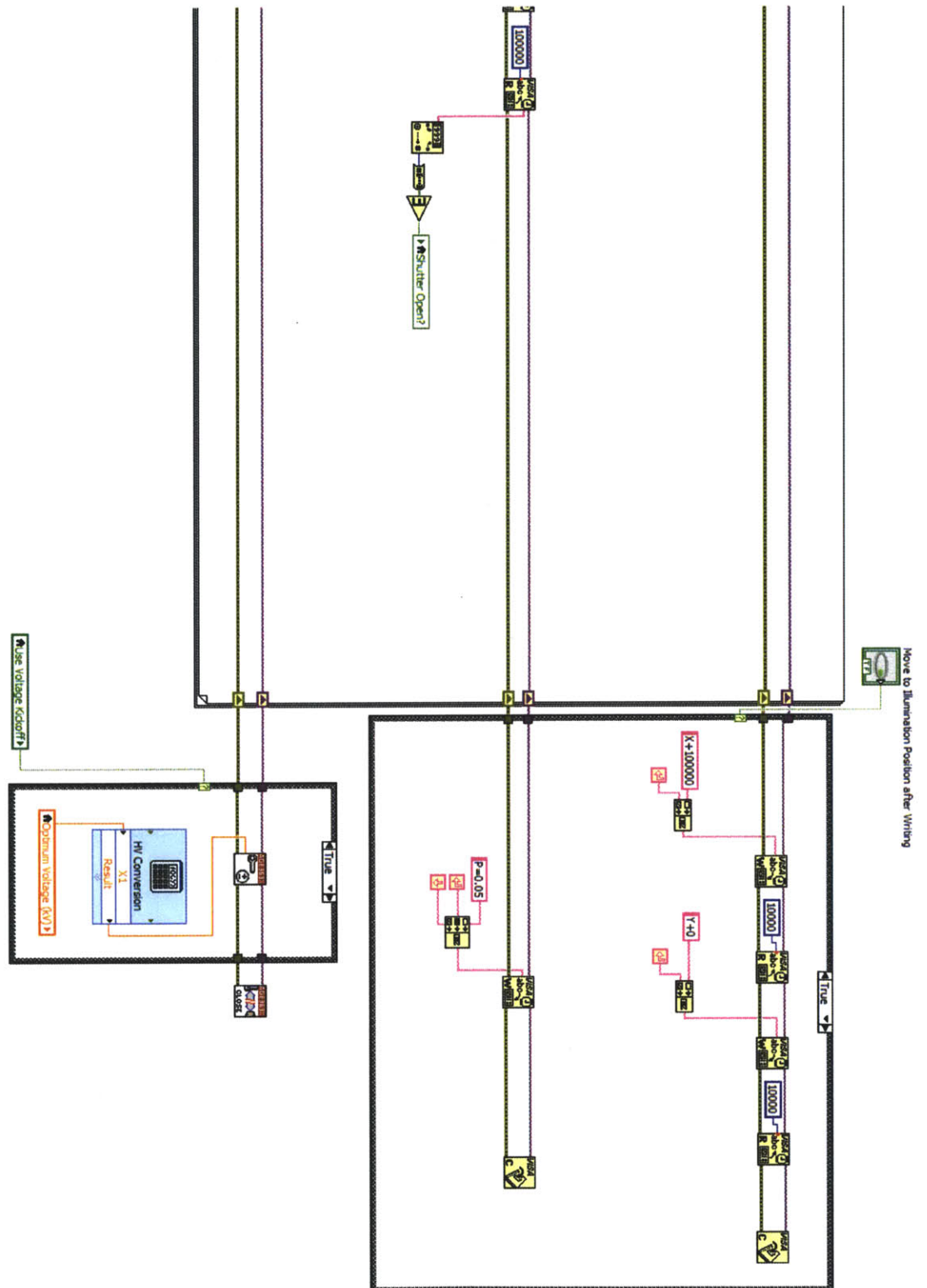
Appendix B

MATLAB Code for Optical Modeling & Simulation

B.1 Fresnel Diffraction via Discrete 2-D Convolution

This function computes the propagation of light via the convolution form of the Fresnel diffraction integral, according to the diffraction geometry pictured in Fig. 1.5.

```
function U1 = fresnelProp(m,U0,z,lambda,fx_u,fy_u,s)
% 2-D Fresnel propagation via convolution of input electric field with free
% space transfer function. m indicates choice of method (0 = angular spectrum,
% 1 = Fresnel approximation), U0 is the input field, z is propagation distance,
% lambda is optical wavelength, and fx_u and fy_u are spatial frequency vectors.

if m == 0 % Use Angular Spectrum method

% Propagation kernel
trans_f=exp(1i*2*pi*(z/lambda)*sqrt(1.-(lambda.*fx_u).^2-(lambda.*fy_u).^2));

% Apply convolution in Fourier domain
if s==0
    fft_field=fftshift(fft2(U0));
else
    fft_field=fft2(U0);
end

h=trans_f.*fft_field;

% Discard evanescent wave components
for i=1:size(U0,1)
    for j=1:size(U0,2)
        constraint=sqrt(fx_u(i).^2+fy_u(j).^2);
```

85

```
            if constraint<(1/lambda);
            else
                h(i,j)=0;
            end
        end
end


% Revert to spatial domain
U1=ifft2(h);

elseif m == 1 % use convolution form of Fresnel approximation

    k = 2 * pi / lambda;
% Propagation kernel for Fresnel approximation
   h = exp(1i * k * z) / (1i * lambda * z) * exp(1i * k / (2 * z) *(fx_u.^2 + fy_u.^2));

% Apply convolution in Fourier domain
    if s==0
        fft_field=fftshift(fft2(og_field));
        trans_f=(fft(h));
    else
        fft_field=fft2(og_field);
        trans_f=fft2(h);
    end

    new_field_fourier=trans_f.*fft_field;

% Revert to spatial domain
    new_field=ifft2(new_field_fourier);

end

end
```

B.2 Telecentric Demagnification via Thin Lens Complex Transmittance

This script computes the optical field incident on a recording medium after a plane wave initialization, modulation with a diffraction grating pattern, and telecentric demagnification via ideal thin cylindrical lenses modeled by phase-only transmittance functions.

```
% Optical model for ideal bilaterally telecentric system
close all;
clear all;

% Define physical and mathematical constants
eps_0 = 8.85e-12;        % Permittivity of free space
c_0 = 299792458;         % Speed of light in vacuum (m/s)
e = 2.718281828;         % Natural logarithmic base

% Define beam parameters
lambda = 532e-9;         % operating wavelength (m)
P0 = 200e-3;              % nominal output power (W)
k = (2 * pi) / lambda;   % wavevector magnitude (1/m)

% Define grid
Nx = 2048;               % number of pixels defined in x-dimension
Ny = 2048;               % number of pixels defined in y-dimension
dim = [Nx, Ny];          % vector specifying overall pixel dimensions

% Create spatial domain
Tx_u1 = 1e-3;
dx_u1 = Tx_u1 / Nx;
vx_u1 = -Tx_u1 / 2:dx_u1:(Tx_u1/2 - dx_u1);
Ty_u1 = 1e-3;
dy_u1 = Ty_u1 / Ny;
vy_u1 = -Ty_u1 / 2:dy_u1:(Ty_u1/2 - dy_u1);
[x_u1, y_u1] = meshgrid(vx_u1, vy_u1);
% Create spatial frequency domain
fx_v_u1 = (-1/Tx_u1 * Nx/2):(1/Tx_u1):(1/Tx_u1 * Nx/2 - 1/Tx_u1);
fy_v_u1 = (-1/Ty_u1 * Ny/2):(1/Ty_u1):(1/Ty_u1 * Ny/2 - 1/Ty_u1);
[fx_u1, fy_u1] = meshgrid(fx_v_u1, fy_v_u1);

% Define grating parameters
Lambda = 35 * dx_u1;

s=0; % Not shifted
```

```
% Find amplitude for single point in initial plane wave field
A0 = sqrt(2 * P0 / (c_0 * eps_0 * Nx * Ny));

% Create finite plane wave
U_p = A0 * ones(Nx,Ny) * exp(pi);

orderStop = zeros(Nx,Ny);
for index1 = 1:Nx
    for index2 = 1:Ny
        if (abs(vy_u1(index1)) < 0.5e-4)
            orderStop(index1,index2) = 1;
        end
    end
end
U_p = U_p .* orderStop;

% Plot irradiance distribution of original plane wave
figure(1);
imagesc(vx_u1, vy_u1, abs(U_p).^2);
xlabel('x (m)');
ylabel ('y (m)');
title('Irradiance distribution of original plane wave');

% Create binary grating
G = .5 * (1 + square(2 * pi / Lambda * (vx_u1 - Lambda / 4), 50));
[Gx_new, Gy_new] = meshgrid(vx_u1, G);
% gy_new = gy_new';

% Plot grating
figure(2);
imagesc(vx_u1, vy_u1, abs(Gy_new));
xlabel('x (m)');
ylabel ('y (m)');
title('Grating distribution');

% Modulate plane wave with grating
U_m = U_p .* Gy_new;
clear U_p; clear Gy_new; clear Gx_new; clear G;

% Plot irradiance distribution after modulation with grating
figure(3);
imagesc(vx_u1, vy_u1, abs(U_m).^2);
xlabel('x (m)');
ylabel ('y (m)');
```

```matlab
title('Irradiance distribution after spatial light modulation');

% Propagate modulated field to first lens via Fresnel diffraction
z_L1 = 10e-6;
U_L1 = fresnelProp(1,U_m,z_L1,lambda,x_u1,y_u1,0);
clear U_m;

% Plot irradiance distribution arriving at first lens
figure(4);
imagesc(vx_u1, vy_u1, abs(U_L1).^2);
xlabel('x (m)');
ylabel ('y (m)');
title('Irradiance distribution arriving at first lens');

% Apply transmissive function for first lens
f1 = 250e-3;
L1 = zeros(Nx,Ny);
for index1 = 1:Nx
    for index2 = 1:Ny
        L1(index1,index2) = exp(-(1i*k)/(2*f1)*(y_u1(index1,index2).^2));
    end
end
U_L1_plus = U_L1 .* L1;
clear U_L1; clear L1;

f2 = 50e-3;
z_L2 = f1 + f2;
z_step = 10e-3;
n_steps = floor(z_L2/z_step);

U_intermediate = U_L1_plus;

% Block diffracted orders from SLM grating to avoid field outside defined
% domain
for index = 1:n_steps

    % Propagate field to intermediate distance via Fresnel diffraction
    z_intermediate = z_step;
  U_intermediate = fresnelProp(1,U_intermediate,z_intermediate,lambda,x_u1,y_u1,1);
    clear U_L1_plus;

    % Plot irradiance distribution arriving at aperture stop
    figure(5);
    imagesc(vx_u1, vy_u1, abs(U_intermediate).^2);
```

```
        xlabel('x (m)');
        ylabel ('y (m)');
        title('Irradiance distribution arriving at aperture stop');


        U_intermediate = U_intermediate .* orderStop;


        % Plot stop distribution
        figure(6);
        imagesc(vx_u1, vy_u1, abs(U_intermediate).^2);
        xlabel('x (m)');
        ylabel ('y (m)');
        title('Stopped irradiance distribution');

end


U_L2 = U_intermediate;


% Plot irradiance distribution arriving at second lens
figure(7);
imagesc(vx_u1, vy_u1, abs(U_L2).^2);
xlabel('x (m)');
ylabel ('y (m)');
title('Irradiance distribution arriving at second lens');

% Apply transmissive function for second lens
L2 = zeros(Nx,Ny);
for index1 = 1:Nx
    for index2 = 1:Ny
        L2(index1,index2) = exp(-(1i*k)/(2*f2)*(y_u1(index1,index2).^2));
    end
end
U_L2_plus = U_L2 .* L2;
clear U_L2; clear L2;

% Propagate field to photorefractive polymer via Fresnel diffraction
z_PR = 5e-3;
U_PR = fresnelProp(1,U_L2_plus,z_PR,lambda,x_u1,y_u1,1);
clear U_L2_plus;

% Plot irradiance distribution arriving at photorefractive polymer
figure(8);
imagesc(vx_u1, vy_u1, abs(U_PR).^2);
xlabel('x (m)');
ylabel ('y (m)');
```

```
title('Irradiance distribution arriving at photorefractive polymer');
```

B.3 Telecentric Imaging System via Point Spread Function of Real Lens System

This script computes the optical field incident on a recording medium after a plane wave initialization, modulation with a diffraction grating pattern, and telecentric demagnification via the real cylindrical lens system used for experiments and modeled using the system point spread function. The point spread function of the imaging system is computed using the ZEMAX optical design suite and imported via file into the MATLAB environment.

```
% Optical model for real bilaterally telecentric system
% Real system modeled by PSF, imported from ZEMAX
close all;
clear all;

% Define physical and mathematical constants
eps_0 = 8.85e-12;              % Permittivity of free space
c_0 = 299792458;              % Speed of light in vacuum (m/s)
e = 2.718281828;              % Natural logarithmic base

% Define beam parameters
lambda = 532e-9;              % operating wavelength (m)
P0 = 2e-3;                    % nominal output power (W)
k = (2 * pi) / lambda;       % wavevector magnitude (1/m)

% Define grid
Nx = 2048;                    % number of pixels defined in x-dimension
Ny = 2048;                    % number of pixels defined in y-dimension
dim = [Nx, Ny];              % vector specifying overall pixel dimensions

% Create spatial domain
Tx_u1 = 1e-3;
dx_u1 = Tx_u1 / Nx;
vx_u1 = -Tx_u1 / 2:dx_u1:(Tx_u1/2 - dx_u1);
Ty_u1 = 1e-3;
dy_u1 = Ty_u1 / Ny;
vy_u1 = -Ty_u1 / 2:dy_u1:(Ty_u1/2 - dy_u1);
[x_u1, y_u1] = meshgrid(vx_u1, vy_u1);
% Create spatial frequency domain
fx_v_u1 = (-1/Tx_u1 * Nx/2):(1/Tx_u1):(1/Tx_u1 * Nx/2 - 1/Tx_u1);
fy_v_u1 = (-1/Ty_u1 * Ny/2):(1/Ty_u1):(1/Ty_u1 * Ny/2 - 1/Ty_u1);
[fx_u1, fy_u1] = meshgrid(fx_v_u1, fy_v_u1);

% Define grating parameters
Lambda = 17e-6;
```

```matlab
s=0; % Not shifted

% Find amplitude for single point in initial plane wave field
A0 = sqrt(2 * P0 / (c_0 * eps_0 * Nx * Ny));

% Create finite plane wave
U_p = A0 * ones(Nx,Ny) * exp(pi);

% orderStop = zeros(Nx,Ny);
% for index1 = 1:Nx
%       for index2 = 1:Ny
%             if (abs(vy_u1(index1)) < 0.5e-4)
%                   orderStop(index1,index2) = 1;
%             end
%       end
% end
% U_p = U_p .* orderStop;

% Plot irradiance distribution of original plane wave
figure(1);
imagesc(vx_u1, vy_u1, abs(U_p).^2);
xlabel('x (m)');
ylabel ('y (m)');
title('Irradiance distribution of original plane wave');

% Create binary grating
G = .5 * (1 + square(2 * pi / Lambda * (vx_u1 - Lambda / 4), 50));
[Gx_new, Gy_new] = meshgrid(vx_u1, G);

% Plot grating
figure(2);
imagesc(vx_u1, vy_u1, abs(Gy_new));
xlabel('x (m)');
ylabel ('y (m)');
title('Grating distribution');

% Modulate plane wave with grating
U_m = U_p .* Gy_new;
clear Gx_new; clear G;

% Plot irradiance distribution after modulation with grating
figure(3);
imagesc(vx_u1, vy_u1, abs(U_m).^2);
```

```
xlabel('x (mm)');
ylabel ('y (mm)');
title('Irradiance distribution after spatial light modulation');

% Propagate modulated field to first lens via Fresnel diffraction
z_L1 = 1e-6;
U_L1 = fresnelProp(1,U_m,z_L1,lambda,x_u1,y_u1,0);
clear U_m;

% Plot irradiance distribution arriving at first lens
figure(4);
imagesc(vx_u1, vy_u1, abs(U_L1).^2);
xlabel('x (m)');
ylabel ('y (m)');
title('Irradiance distribution arriving at first lens');

% Apply PSF of imaging system via multiplication in Fourier domain
load('DEFAULT.mat');
PSF=imresize(DEFAULT,[2048,2048]);
PSF2=PSF(2:245,:);
PSF=zeros(Nx,Ny);
PSF(903:1146,:) = PSF2;
U_L2_plus = fftshift(ifft2((fftshift(fft2(U_L1)).*fftshift(fft2(PSF)))));
clear PSF2;

% Plot point spread function
figure(5);
imagesc(vx_u1, vy_u1, PSF);
xlabel('x (m)');
ylabel ('y (m)');
title('Point spread function');

% Create scaled spatial domain
M = 1/5;
vx_u1 = M .* vx_u1;
vy_u1 = M .* vy_u1;
[x_u1, y_u1] = meshgrid(vx_u1, vy_u1);
% Create spatial frequency domain
fx_v_u1 = (-1/Tx_u1 * Nx/2):(1/Tx_u1):(1/Tx_u1 * Nx/2 - 1/Tx_u1);
fy_v_u1 = (-1/Ty_u1 * Ny/2):(1/Ty_u1):(1/Ty_u1 * Ny/2 - 1/Ty_u1);
[fx_u1, fy_u1] = meshgrid(fx_v_u1, fy_v_u1);

% Plot irradiance distribution emerging from PSF convolution
figure(6);
```

```
imagesc(vx_u1, vy_u1, abs(U_L2_plus).^2);
xlabel('x (m)');
ylabel ('y (m)');
title('Irradiance distribution after PSF convolution');

% Propagate field to photorefractive polymer via Fresnel diffraction
z_PR = 1e-6;
U_PR = fresnelProp(1,U_L2_plus,z_PR,lambda,x_u1,y_u1,1);

% Plot irradiance distribution arriving at photorefractive polymer
figure(7);
imagesc(vx_u1, vy_u1, abs(U_PR).^2);
xlabel('x (m)');
ylabel ('y (m)');
title('Irradiance distribution arriving at photorefractive polymer');
```

B.4 Photorefractive Polymer Exposure

This script computes the 3-D volume phase hologram resulting from exposure to an interferogram as computed using the presented telecentric imaging system models.

```
% Calculate refractive index modulation in PR material
% \Delta n ~=~ \alpha \tau |E|^2, where \alpha is a material constant, \tau
% is exposure time, |E|^2 is electric field amplitude squared
% U_PR is field arriving at PR material

% PR material parameters
T = 100e-6;

% Solve for spacing in z
delZ = (Lambda * f2/f1)^2 / (2 * pi * lambda)

% Initialize PR grid
N = ceil(T / delZ + 1)
PR_fields = zeros(Nx,Ny,N);
PR_modulation = zeros(Nx,Ny,N);
avgModulation = zeros(1,N);

% Solve for fields at depths in PR material
alpha = 1e-1;
t = 10;

for index = 1:N
    disp('Solving for field in PR material at depth:');
    index
    if index == 1
        PR_fields(:,:,index) = U_PR;
    else
      PR_fields(:,:,index) = fresnelProp(1,U_PR,delZ*(index-1),lambda,x_u1,y_u1,1);
    end
    PR_modulation(:,:,index) = alpha * t * abs(PR_fields(:,:,index)).^2;

    % Plot refractive index modulation within PR material
    figure(9);
    imagesc(vx_u1, vy_u1, PR_modulation(:,:,index));
    xlabel('x');
    ylabel ('y');
    title('Refractive index modulation');
end
```

B.5. Grating Diffraction via Thin Phase Grating Decomposition and Iterative Fresnel Propagation

This script computes the scattering resulting from diffraction of a read-out beam via the recorded volume phase hologram using the thin-grating decomposition method presented by Alferness [39,41].

```
% PR_modulation contains the refractive index modulation distribution

% Define beam parameters
lambda = 632.8e-9;          % operating wavelength (m)
P0 = 20e-3;                 % nominal output power (W)
k = (2 * pi) / lambda;     % wavevector magnitude (1/m)

% Create Gaussian read-out beam
theta_div = 0.25;                                    % FWHM divergence angle (degrees)
w0 = lambda / (pi * (theta_div/1.18) * pi / 180);   % Beam waist size
U_gaussian = exp(-(x_u1.^2 + y_u1.^2) / w0.^2);
nu_0 = 377;                % Characteristic Impedance of Free Space (Ohms)
% Normalization Constant
A = sqrt((P0 / ((sum(sum(abs(U_gaussian).^2 * dx_u1 * dy_u1)))) * 2 * nu_0));
U_gaussian = A * U_gaussian;

% Plot read-out beam irradiance distribution
figure(10);
imagesc(vx_u1, vy_u1, abs(U_gaussian).^2);
xlabel('x');
ylabel ('y');
title('Irradiance distribution incident on photorefractive polymer');

% Initialization
t = zeros(Nx,Ny);
U_plus = zeros(Nx,Ny);
U_minus = U_gaussian;

% Find field emerging from PR material via TGDM
for index = 1:N
    disp('Solving for diffraction from decomposed grating in PR material at depth:');
        index
        % t_i = exp(j * 2 * pi * delN * delZ / lambda);
        t = exp(1i * 2 * pi * PR_modulation(:,:,index) * delZ / lambda);
        U_plus = U_minus .* t;
        if index == 1
            U_minus = fresnelProp(1,U_plus,delZ,lambda,x_u1,y_u1,0);
```

```
    else
        U_minus = fresnelProp(1,U_plus,delZ,lambda,x_u1,y_u1,1);
    end
end

U_D = fresnelProp(U_minus,delZ,lambda,x_u1,y_u1,1);

% Plot irradiance distribution emerging from photorefractive polymer
figure(11);
imagesc(vx_u1, vy_u1, abs(U_D).^2);
xlabel('x (m)');
ylabel ('y (m)');
title('Irradiance distribution emerging from photorefractive polymer');

% Find diffracted field at a screen
z_S = 0.3e-3;
U_screen = fresnelProp(1,U_D,z_S,lambda,x_u1,y_u1,1);

% Plot irradiance distribution at screen
figure(12);
imagesc(vx_u1, vy_u1, abs(U_screen).^2);
xlabel('x (m)');
ylabel ('y (m)');
title('Irradiance distribution at screen');
```